

# Highly Ionized High-Velocity Clouds toward PKS 2155–304 and Markarian 509

Joseph A. Collins, J. Michael Shull<sup>1</sup>

*University of Colorado, CASA, Department of Astrophysical & Planetary Sciences,  
Campus Box 389, Boulder, CO 80309*

and

Mark L. Giroux

*East Tennessee State University, Department of Physics & Astronomy, Box 70652,  
Johnson City, TN 37614*

## ABSTRACT

To gain insight into four highly ionized high-velocity clouds (HVCs) discovered by Sembach et al. (1999), we have analyzed data from the *Hubble Space Telescope* (*HST*) and *Far Ultraviolet Spectroscopic Explorer* (*FUSE*) for the PKS 2155–304 and Mrk 509 sight lines. We measure strong absorption in O VI and column densities of multiple ionization stages of silicon (Si II/III/IV) and carbon (C II/III/IV). We interpret this ionization pattern as a multiphase medium that contains both collisionally ionized and photoionized gas. Toward PKS 2155–304, for HVCs at  $-140$  and  $-270$  km s<sup>-1</sup>, respectively, we measure  $\log N(\text{O VI}) = 13.80 \pm 0.03$  and  $\log N(\text{O VI}) = 13.56 \pm 0.06$ ; from Lyman series absorption, we find  $\log N(\text{H I}) = 16.37^{+0.22}_{-0.14}$  and  $15.23^{+0.38}_{-0.22}$ . The presence of high-velocity O VI spread over a broad (100 km s<sup>-1</sup>) profile, together with large amounts of low-ionization species, is difficult to reconcile with the low densities,  $n_e \approx 5 \times 10^{-6}$  cm<sup>-3</sup>, in the collisional/photoionization models of Nicastro et al. (2002), although the HVCs show a similar relation in  $N(\text{Si IV})/N(\text{C IV})$  versus  $N(\text{C II})/N(\text{C IV})$  as high- $z$  intergalactic clouds. Our results suggest that the high-velocity O VI in these absorbers do not necessarily trace the WHIM, but instead may trace HVCs with low total hydrogen column density. We propose that the broad high-velocity O VI absorption arises from shock ionization, at bowshock interfaces produced from infalling clumps of gas with velocity shear. The similar ratios of high ions for HVC Complex C and these highly ionized HVCs suggest a common production mechanism in the Galactic halo.

---

<sup>1</sup>Also at JILA, University of Colorado and National Institute of Standards and Technology.

*Subject headings:* Galaxy: halo — ISM: clouds — ISM: abundances — quasars: absorption lines

## 1. INTRODUCTION

The high-velocity clouds (HVCs; Wakker & van Woerden 1997) seen in H I 21 cm emission are characterized by significant deviation from a simple model of differential Galactic rotation. Although they are thought to reside in the Galactic halo, their origin within the context of galaxy assembly is not well understood. The fact that a large fraction of HVCs exhibit negative velocity centroids in the local standard of rest (LSR), and the need to explain the metallicity distribution of long-lived stars in the solar neighborhood (Flynn & Morell 1997), have motivated the suggestion that these HVCs represent the accretion of low-metallicity gas onto the Galaxy (Wakker et al. 1999; Collins, Shull, & Giroux 2003, hereafter CSG). Negative velocity HVCs may be condensed remnants of a “Galactic fountain” (Shapiro & Field 1976; Bregman 1980) now returning to the disk.

An alternate, but controversial hypothesis places some of the HVCs at locations in the Local Group (Blitz et al. 1999), perhaps 500 kpc distant, and identifies the compact HVCs (CHVCs) in particular as a population of dwarf-type galaxies at large distance (Braun & Burton 1999). However, evidence supporting this hypothesis has not been forthcoming, since both a stellar component to the CHVCs (Simon & Blitz 2002; Hopp, Schulte-Ladbeck, & Kerp 2003) and similar H I clouds in nearby groups (Zwaan 2001) have yet to be detected. Recent H $\alpha$  detections of HVCs and CHVCs indicate that many of these objects are within a  $\sim 40$  kpc radius of the Galaxy (Putman et al. 2003). In addition, models suggest that many CHVCs at Local Group distances would have unreasonably large total masses, summing the neutral, ionized, and dark matter (Maloney & Putman 2003). This discussion of HVC location within the Galaxy halo or Local Group has expanded to include a population of O VI HVCs (Sembach et al. 2003; Nicastro et al. 2003). In a specific instance, abundance studies of HVC Complex C with the *Far Ultraviolet Spectroscopic Explorer (FUSE)* and *Hubble Space Telescope (HST)* suggest that this gas is an infalling low-metallicity cloud mixing with gas of Galactic origin (CSG; Tripp et al. 2003).

An additional consideration is the HVC hot gas content. Cosmological simulations predict that the collapse of gas during galaxy formation should produce significant amounts of shock-heated gas (Cen & Ostriker 1999) in the low-redshift intergalactic medium (IGM), the so-called warm-hot IGM or WHIM. Temperatures of this shocked gas would be  $10^5 - 10^7$  K, resulting in significant ionization fractions of O VI, O VII, and, if the temperature is sufficiently high, O VIII. A goal of recent *FUSE* surveys of high-velocity O VI has been

to investigate the interaction of HVCs with the WHIM and hot gas in the Galactic halo (Sembach et al. 2003; Indebetouw & Shull 2004). If HVCs are remnants of Local Group formation, then the associated O VI may trace collisionally ionized gas at the cloud/IGM interface.

In this paper, we use new data from the E140M echelle on the *Space Telescope Imaging Spectrograph* (STIS) to assess the physical characteristics of a class of “highly ionized HVCs”. These clouds were discovered by Sembach et al. (1995) and further defined by Sembach et al. (1999, hereafter S99). Using data from the *Goddard High Resolution Spectrograph* (GHRS), S99 studied four of these HVCs along the lines of sight toward the AGN PKS 2155–304 and Mrk 509. These absorbers exhibited strong C IV absorption accompanied by little or no absorption in low ions. High-velocity H I emission was detected in an area encompassing  $\sim 2^\circ$  near the sight lines, but no H I emission could be detected in the sight lines themselves down to sensitivity levels of  $N(\text{H I}) \gtrsim 10^{18} \text{ cm}^{-2}$ . In addition, H I emission associated with the Galactic Center Negative (GCN) clouds can be detected at similar velocities to the HVCs within  $\sim 5^\circ$  of the sight lines, indicating a possible association between the HVCs and the GCN clouds. The column density constraints from the GHRS data were successfully modeled as arising from an extragalactic QSO-type radiation field. The resulting densities, pressures, and sizes of the clouds suggested to S99 that these HVCs were most likely located in the Local Group or distant Galactic Halo, and that the highly ionized gas traces the outer, low-density regions of the HVCs.

However, O VI has recently been detected in these HVCs (Sembach et al. 2003) at column densities well above any reasonable prediction from photoionization models, indicating a contribution from other ionization sources. Nicastro et al. (2002) detected zero-redshift O VII X-ray absorption in the PKS 2155–304 sight line, and identified it as a filament of WHIM. Because the resolution of the X-ray data is poor ( $\sim 600 \text{ km s}^{-1}$  at  $20 \text{ \AA}$ ) relative to the UV data, it is not possible to distinguish Galactic absorption from the HVC absorption in those data.

Nevertheless, Nicastro et al. (2002) model the X-ray absorption lines *and* the high-velocity O VI absorption as arising in the same low-density ( $n_e \approx 5 \times 10^{-6} \text{ cm}^{-3}$ ) collisionally ionized WHIM component. They suggest that the clouds are primarily collisionally ionized, with a contribution from photoionization by the extragalactic UV/X-ray background. This interpretation requires a large photoionization parameter,  $U = n_\gamma/n_H$ , and a low gas density,  $n_H \approx 5 \times 10^{-6} \text{ cm}^{-3}$ . The large implied cloud sizes suggest that the PKS 2155–304 HVCs are at Local Group distances. This hypothesis has important astronomical consequences. The FUSE survey of HVCs (Sembach et al. 2003) found high-velocity O VI over a covering fraction  $f_{\text{sky}} = 0.60\text{--}0.85$ , down to columns  $\log N(\text{O VI}) = 13.95$ . For an assumed metallicity,

(O/H) =  $5.45 \times 10^{-5}$  (Holweger 2001), that is 10% of solar, and  $T = 10^{5.45}$  K gas temperature (ionization fraction,  $f_{\text{OVI}} = 0.2$ ), this corresponds to an ionized hydrogen column density  $N(\text{H}^+) = 8 \times 10^{18} \text{ cm}^{-2}$ . This implies a total gas mass  $M_{\text{hot}} \approx (10^{10} M_{\odot}) f_{\text{sky}} d_{100}^2$  at mean distance (100 kpc)  $d_{100}$ . Placing the O VI HVCs at  $d \sim 1$  Mpc would then result in masses exceeding that of the entire Milky Way galaxy.

Heckman et al. (2002) also cast doubt on the “Local Group” interpretation by pointing out that the entire population of O VI absorbers, including those of known IGM clouds, can be modeled as “cooling layers” of gas, with initial temperature  $T \approx 10^6$  K. In such a non-photoionization scenario, the large cloud sizes and low densities are unnecessary, and the HVCs could instead trace gas in the Galactic halo.

With the recent acquisition of *HST*/STIS echelle spectra for both PKS 2155–304 (Shull, et al. 2003) and Mrk 509 (Kraemer et al. 2003) comes the opportunity to reexamine the highly-ionized HVCs toward these targets. The STIS has superior sensitivity, resolution, and spectral coverage to GHRS, allowing a more thorough investigation of a wider variety of absorption lines. In addition to providing important information on O VI, N II, and C III, *FUSE* spectra include coverage of H I absorption lines from Ly $\beta$  down to the hydrogen Lyman limit (Moos et al. 2000). If the data quality is high, the higher Lyman lines can be used to determine  $N(\text{H I})$  for the HVCs, which is critical for restricting parameter space in ionization models. For PKS 2155–304, we are able to measure  $\log N(\text{H I})$  of the HVCs to  $\pm 0.2 - 0.3$  dex.

Using measured column densities of multiple ion species, we investigate the physical conditions and characteristics of four of these highly-ionized HVCs toward two AGN. In light of the “Local Group hypothesis” for HVC distances, we attempt to determine whether these clouds are extragalactic objects or associated with the Galactic halo. Because of the substantial O VI column densities detected, we suggest that O VI and other high ions arise in collisionally ionized gas. In addition, the presence of highly-ionized species allows us to investigate the interaction of HVCs with the IGM or Galactic halo. Our method of processing of the raw data is discussed in § 2. The column density measurements are presented in § 3. In § 4, we discuss the results, present models for the ionization of these clouds, and compare the observed column density ratios to measurements of multiple ions of carbon (C II/III/IV) and silicon (Si II/III/IV) in the IGM at high and low redshift.

## 2. FUSE AND HST-STIS DATA

Data for these sight lines consist of *HST*/STIS echelle and *FUSE* spectra obtained from the Multimission Archive (MAST) at the Space Telescope Science Institute. The *HST* data for PKS 2155-304 were obtained in a ten-orbit STIS exposure as part of GO Program 8125 in Cycle 8 (Shull et al. 2003). The *FUSE* data were obtained in observations by the *FUSE* Science Team. A summary of the observations is shown in Table 1.

Calibrated *FUSE* spectra were extracted by passing raw data through the CALFUSE Version 2.2 reduction pipeline. In order to improve the signal-to-noise ratio (S/N), both “day” and “night” photons are included in the final calibrated *FUSE* spectra. The inclusion of day photons leads to strong airglow contamination of certain neutral interstellar lines near the LSR. Such airglow contamination is irrelevant for the purpose of investigating high-velocity absorption in this study. Individual exposures were then co-added and weighted by their exposure times, to yield a final *FUSE* spectrum. To further improve S/N, the data were rebinned over 5 pixels. *FUSE* spectra have a resolution over the FUSE bandpass (912–1187 Å) of about  $20 \text{ km s}^{-1}$  ( $\sim 10$  pixels), and as a result the data are oversampled at that resolution. To set the absolute wavelength scale, the centroid of Galactic H I 21-cm emission was compared and aligned to various Galactic absorption lines in the *FUSE* bandpass, such as those of Si II ( $\lambda 1020.70$ ), O I ( $\lambda 1039.23$ ), Ar I ( $\lambda\lambda 1048.22, 1066.66$ ), Fe II ( $\lambda\lambda 1125.45, 1144.94$ ), N I ( $\lambda 1134.17$ ), and various H<sub>2</sub> Lyman bands.

The *HST*/STIS observations were taken in the E140M echelle mode, providing a wavelength coverage of 1150–1700 Å at  $7 \text{ km s}^{-1}$  resolution. A final STIS spectrum was obtained by co-adding individual exposures, weighted by their exposure times and rebinning the data over 3 pixels. An absolute wavelength scale was obtained as for the *FUSE* spectrum, matching the Galactic H I emission peak to absorption features of N I ( $\lambda 1199.55$ ), S II ( $\lambda\lambda 1250.58, 1253.80, 1259.52$ ), O I ( $\lambda 1302.17$ ), and Si II ( $\lambda\lambda 1304.37, 1526.71$ ). We estimate the absolute wavelength scales of both the STIS and *FUSE* data to be accurate to within  $\sim 10 \text{ km s}^{-1}$ .

## 3. COLUMN DENSITY MEASUREMENTS

In both the PKS 2155–304 and Mrk 509 sight lines, high velocity metal-line absorption is clearly present (see Figures 1 and 6). In order to ascertain characteristics and physical conditions in these clouds, it is important to determine column densities of the various ion species. In the few cases where multiple lines of one species can be measured, we use a curve-of-growth (CoG) fitting procedure to measure column densities. More commonly, we measure columns with the apparent optical depth (AOD) method. Though a CoG fit is the more

robust method of determining column densities, the AOD method is valid for unsaturated lines (Savage & Sembach 1991). Line saturation can be difficult to detect, particularly if such saturation is unresolved. However, we can test for the presence of unresolved saturation in the case of doublets (e.g., the C IV and Si IV doublets) where the implied optical depths of the weak and strong lines can be compared. In cases of saturated doublets we use a CoG fit to determine the column density. The optical depth of absorption at velocity  $v$  is given by,

$$\tau_v = -\ln[I_n(v)] , \quad (1)$$

where  $I_n(v)$  is the observed normalized intensity at velocity  $v$ . Individual line profiles were normalized by fitting low-order polynomials to the continuum immediately surrounding the line in question. Typically, we fit the continuum  $\pm 3\text{--}5 \text{ \AA}$  about the rest wavelength of the line, although in a number of cases spurious absorption near the line required the use of a much larger region for continuum measurement. The column density is then given by integrating  $\tau_v$  over the velocity range of the absorption feature,

$$N_{AOD}(\text{cm}^{-2}) = \left( \frac{3.767 \times 10^{14}}{f\lambda} \right) \sum_v \tau_v \Delta v , \quad (2)$$

where  $\Delta v$  is the bin size in  $\text{km s}^{-1}$  and values of the oscillator strength,  $f$ , and the rest wavelength,  $\lambda$  (in  $\text{\AA}$ ), are from D. C. Morton (2004, in preparation). Measurements for the HVCs in the PKS 2155–304 and Mrk 509 sight lines are discussed individually in the following sections.

### 3.1. PKS 2155–304

Absorption-line profiles of metal ions in the *FUSE* and STIS bandpass are shown in Figure 1. As in the GHRS data presented by S99, the profiles show two distinct high-velocity components. The stronger component occupies the velocity range of  $-200 < V_{LSR} < -95 \text{ km s}^{-1}$  (centered at  $-140 \text{ km s}^{-1}$ ) while the other is located in the range  $-310 < V_{LSR} < -200 \text{ km s}^{-1}$  (centered at  $-270 \text{ km s}^{-1}$ ). Each of the components show highly ionized absorption in C IV, Si IV, and O VI, while only the  $-140 \text{ km s}^{-1}$  component shows singly-ionized absorption in C II and Si II. The extent of the singly ionized and highly ionized absorption lines are noticeably different for the  $-140 \text{ km s}^{-1}$  component. Figure 2 shows normalized absorption profiles of carbon and silicon species. Lines of C II and Si II are confined to the range  $-165 < V_{LSR} < -95 \text{ km s}^{-1}$ , while absorption from the more highly-ionized species extends to higher velocities. This difference hints at a possible multi-component structure to the  $-140 \text{ km s}^{-1}$  component, with the highly-ionized species tracing a more extended halo

than the less ionized core. The profile of C III absorption may be a reflection of saturation instead of a truly flat column density distribution.

Table 2 shows measured equivalent widths and column densities for each of the components in the PKS 2155–304 sight line. For the  $-140 \text{ km s}^{-1}$  component, the measurement of multiple lines of Si II and C II allows us to use a CoG to measure column densities, or their upper limits for the neutral and singly ionized metal species. The three Si II and two C II lines are best fitted by a CoG with doppler parameter  $b = 10.3 \text{ km s}^{-1}$ , as shown in Figure 3. The profiles of C III and Si III for the  $-140 \text{ km s}^{-1}$  component show evidence of possible saturation and, as a result, their measured column densities place lower limits on the actual columns. Within the errors, the column densities presented in Table 2 are consistent with the columns derived from GHRIS data presented by S99. The quality of the GHRIS data led S99 to conclude, however, that these clouds show little or no detectable low ion absorption. Our results indicate measurable columns of low-ionization species for the  $-140 \text{ km s}^{-1}$  component (in H I, C II, and Si II), as well as for the  $-270 \text{ km s}^{-1}$  component (in H I, but only upper limits on C II or Si II).

The *FUSE* SiC channel data quality is sufficient to obtain equivalent widths for many H I Lyman-series absorption lines. Profiles of H I absorption lines in this sight line are shown in Figure 4. The H I column of the  $-270 \text{ km s}^{-1}$  component is sufficiently low that unsaturated absorption can be detected in Ly $\gamma$ , with the component eventually becoming undetectable at Ly $\theta$ . Owing to blending with saturated Galactic H I absorption, only lines from Ly $\eta$  through Ly $\lambda$  are useful for measuring the H I column of the  $-140 \text{ km s}^{-1}$  component. Equivalent width measurements of the H I Lyman lines for the HVC components are shown in Table 3, for four and five H I lines for the  $-270$  and  $-140 \text{ km s}^{-1}$  components, respectively. We employed a CoG analysis (Fig. 5) to determine the corresponding H I column densities of these components,  $\log N(\text{H I}) = 16.37_{-0.14}^{+0.22}$  for the  $-140 \text{ km s}^{-1}$  component and  $\log N(\text{H I}) = 15.23_{-0.22}^{+0.38}$  for the  $-270 \text{ km s}^{-1}$  component. This is a significant improvement over the work of S99, where only an upper limit could be determined based on single-dish H I emission data. These low H I HVC column densities show why no 21-cm emission was detected.

### 3.2. Mrk 509

Profiles of metal ion absorption lines observed in the *FUSE* and STIS data are shown in Figure 6. The data quality is not as good as that for PKS 2155–304, but high-velocity absorption can be detected. As with PKS 2155–304, the profiles show two distinct high-velocity components. In the Mrk 509 sight line, however, the stronger component appears at higher velocity,  $-355 < V_{LSR} < -260 \text{ km s}^{-1}$  (centered at  $-300 \text{ km s}^{-1}$ ), than the

weak component, which can only be detected at the  $3\sigma$  level in a few absorption lines. The weak component is most obvious in C IV  $\lambda 1548.20$  and Si III  $\lambda 1206.50$ . These lines are used to establish an integration range of  $-260 < V_{LSR} < -200$  km s $^{-1}$  (centered at  $-240$  km s $^{-1}$ ) for the weak component. The O VI  $\lambda 1031.93$  absorption from the  $-240$  km s $^{-1}$  component is contaminated by weak absorption from the L(6-0) P(3) Galactic H $_2$  line. The nearby L(7-0) P(3) line has a similar oscillator strength to the L(6-0) P(3) line. To remove this contamination, we inferred the optical depth of the contaminating line by scaling the integrated  $\tau_v$  of the Galactic H $_2$  L(7-0) P(3) line by its relative value of  $f\lambda$ . The line width of the Galactic H $_2$  L(7-0) P(3) is then used to subtract off the appropriate integrated  $\tau_v$  for the contaminating absorption. The resulting O VI profile looks reasonable, although the removal of the H $_2$  line has effectively smoothed over any possible small-scale structure.

The *FUSE* SiC channel data are so poor that we could not obtain measurements of lines below 1000 Å or between 1080–1100 Å. Thus, our results do not include column density measurements based on N II  $\lambda 1083.994$ , C III  $\lambda 977.020$ , or the H I Lyman lines. The lack of an H I measurement is perhaps most critical, and we were unable to improve on the upper limit from single-dish H I emission data of  $\log N(\text{H I}) < 17.69$  established by Sembach et al. (1995).

Measured equivalent widths and column densities for each of the high-velocity components in the Mrk 509 sight line are shown in Table 4. The column density pattern is similar to the HVCs in the PKS 2155–304 sight line. The core of the Si III  $\lambda 1206.500$  profile for the  $-300$  km s $^{-1}$  component is likely saturated, and the measured column density should be considered a lower limit. Although saturation is not apparent in the C IV and Si IV profiles, it is possible that unresolved saturation can be an issue, since the weak lines give  $\sim 0.1$  dex larger column densities for the  $-300$  km s $^{-1}$  component. In order to test for unresolved saturation, we compared the profiles of the weak and strong lines in the C IV and Si IV doublets. If saturation were an issue, the AOD method should give a larger and more peaked column density for the weak line than for the optically thicker strong line. Figure 7 shows the normalized column density profiles of the C IV and Si IV doublets for the  $-300$  km s $^{-1}$  component. Clearly, unresolved saturation may be present, since the profiles from the weaker lines of the doublets are more peaked between  $-300$  and  $-280$  km s $^{-1}$ . Due to the presence of saturation, a CoG fit to the doublets is used to measure the column densities of C IV and Si IV. Since the feature at  $-350$  km s $^{-1}$  in the Si IV  $\lambda 1402.770$  profile is not observed in the Si IV  $\lambda 1393.755$  profile, we suspect that this feature is a result of spurious absorption in the integration range. Therefore, absorption from this feature is not included in the  $W_\lambda$  measurement of Si IV  $\lambda 1402.770$ .



## 4. DISCUSSION

### 4.1. Column Density Ratios

An obvious characteristic of these HVCs is their strong absorption in highly-ionized species (C IV, Si IV). Furthermore, except for the  $-140 \text{ km s}^{-1}$  component (PKS 2155–304), the column densities of singly-ionized and neutral species are quite low or below the detection limit. There are few HVCs that have been similarly studied with both *FUSE* and *HST*/STIS spectra. One well-studied case is the sight line toward PG 1259+593, which probes the extended HVC Complex C (Richter et al. 2001; CSG). We have gone back to the data for PG 1259+593 and measured the column densities of the common high ions<sup>2</sup>. Although the H I column density of Complex C derived from Effelsberg single-dish 21-cm data ( $9'$  beam size) along that sight line is several orders of magnitude larger than for the highly ionized HVCs,  $\log N(\text{H I}) = 19.92_{-0.01}^{+0.01}$  (Wakker et al. 2001), the measured column densities of C IV, Si IV, and O VI are within an order of magnitude of those for the PKS 2155–304 and Mrk 509 HVCs.

Table 5 perhaps best illustrates the similarities and differences between these highly-ionized HVCs and Complex C, listing various logarithmic column density ratios. In low-to-high ion ratios, the highly-ionized HVCs have values smaller than Complex C by  $\sim 10^3$  to  $10^4$  in  $N(\text{H I})/N(\text{O VI})$  and  $\sim 10^2$  in  $N(\text{Si II})/N(\text{Si IV})$ . However, the highly-ionized HVCs and Complex C show similar ratios involving only the high ions. An exception is the ratio  $N(\text{C IV})/N(\text{Si IV})$  where the value for Complex C is lower than for the highly-ionized HVCs. The value for Complex C,  $\log[N(\text{C IV})/N(\text{Si IV})] = 0.59_{-0.15}^{+0.12}$ , is similar to that observed for gas within the disk or low halo,  $\log[N(\text{C IV})/N(\text{Si IV})] = 0.58_{-0.30}^{+0.18}$  (Sembach, Savage, & Tripp 1997), whereas the values for the highly-ionized HVCs are slightly larger. In addition, the weaker of the highly-ionized HVC components (the  $-270 \text{ km s}^{-1}$  component toward PKS 2155–304 and the  $-240 \text{ km s}^{-1}$  component toward Mrk 509) show larger values of  $N(\text{C IV})/N(\text{Si IV})$  than for the stronger components. Interestingly, the ratio  $N(\text{O VI})/N(\text{C IV})$  shows little difference between the highly-ionized HVCs and Complex C, as well as between the individual HVC components themselves. Fox et al. (2004) find that the high-ion ratios in Complex C are consistent with ionization at conductive or turbulent interfaces between the cloud core and a surrounding hot medium. The similar high-ion ratios for the highly ionized HVCs and Complex C may indicate that these objects share a common production mechanism for the C IV and O VI.

---

<sup>2</sup>The column densities of highly-ionized species associated with Complex C in the PG 1259+593 sight line are:  $\log N(\text{C IV}) = 13.23_{-0.08}^{+0.06}$ ;  $\log N(\text{N V}) < 13.16$ ;  $\log N(\text{O VI}) = 13.54_{-0.05}^{+0.05}$ ;  $\log N(\text{Si IV}) = 12.64_{-0.13}^{+0.10}$ . The measurements were made with the AOD method using the techniques described in CSG.

## 4.2. Comparisons with the IGM

As demonstrated in the previous section, the column density ratios involving the low-ions are unlike those of gas normally associated with the Galaxy. In this section, we compare the observations to those of the IGM. Characteristics of IGM gas are diverse, and we can compare these observations to absorbers at both high- and low-redshift. The values of  $N(\text{Si IV})/N(\text{C IV})$  in these HVCs are similar to values typical for Ly $\alpha$  forest clouds at  $z \approx 3$ , for example those studied by Songaila & Cowie (1996; hereafter SC). Figure 8 shows a diagnostic diagram of  $N(\text{Si IV})/N(\text{C IV})$  versus  $N(\text{C II})/N(\text{C IV})$  for the SC data. The large circles denote data for the four HVC components observed in the PKS 2155–304 and Mrk 509 sight lines. Clearly, the HVCs show values of  $N(\text{Si IV})/N(\text{C IV})$  similar to those of the SC sample. The same can be said for the  $N(\text{C II})/N(\text{C IV})$  ratio for three of the HVC components. The  $-140 \text{ km s}^{-1}$  component towards PKS 2155–304, however, has a value of  $N(\text{C II})/N(\text{C IV})$  more than twice as large as any of the Ly $\alpha$  forest clouds in the SC sample. Though the value of  $N(\text{Si IV})/N(\text{C IV})$  for this HVC is similar to that of the  $z \sim 3$  Ly $\alpha$  forest, it contains higher fractions of low-ionization species (C II) than typically associated with the IGM.

At low-redshift, Tripp et al. (2002) observed metal ions in two Ly $\alpha$  absorbers in the 3C 273 sight line at redshifts in the vicinity of the Virgo cluster. One of the absorbers shows metal absorption in only O VI and is identified by the authors as possibly tracing the WHIM. The other absorber shows absorption in Si II, Si III, and C II, although no absorption is seen in higher ionization species. The authors identify this cloud as a possible Virgo analog to HVCs near the Milky Way. This absorber has a lower limit,  $\log [N(\text{C II})/N(\text{C IV})] > 0.24$ , indicating that it may have similar properties to the  $-140 \text{ km s}^{-1}$  component towards PKS 2155–304, but at lower H I column density.

Nicastro et al. (2002, 2003) interpret the high-velocity O VI (FUSE) detection towards PKS 2155–304 and many other sight lines as tracing the WHIM in the Local Group. Their hypothesis is based on the detection of O VII/O VIII absorption at  $z = 0$  and the narrowing of the O VI velocity distribution when converted to a Local Group standard of rest. Possible detections of the WHIM at higher redshifts have been reported in O VII and O VIII (Fang et al. 2002; Mathur, Weinberg, & Chen 2003), although many of those results have not been confirmed (Rasmussen, Kahn, & Paerels 2003). The high-velocity O VI in the Nicastro et al. picture would be at high temperature ( $T \gtrsim 10^5 \text{ K}$ ), and significant amounts of O VII and O VIII could be present, which are not only difficult to detect but difficult to resolve in X-ray data. Nevertheless, the presence of large amounts of low ionization species in the PKS 2155–304 HVCs is incompatible with the low densities in the collisional/photoionized models of Nicastro et al. (2002). This implies, at least for the HVCs towards PKS 2155–304

and Mrk 509, that the high-velocity O VI do not necessarily trace the WHIM, but instead may trace HVCs with low total hydrogen column density. It is possible that some of the C IV, Si IV, and lower ions could arise from thermal instability in cooling WHIM gas. However, this scenario may be inconsistent with the broad O VI velocity profiles.

### 4.3. Modeling the Ionization Pattern in HVCs

As indicated above, the HVCs toward PKS 2155–304 and Mrk 509 show column density ratios unlike gas associated with the Galactic halo. Although the H I column densities are considerably higher, Galactic halo gas typically has much stronger absorption from low ions than high ions (Sembach & Savage 1992). These HVCs are also distinguished (S99) from Galactic or low halo gas by their high values of  $N(\text{C IV})/N(\text{Si IV}) > 5$ . In order to examine the ionization characteristics of these HVCs and assess their possible origin, we have performed a series of model calculations which are then constrained by the observed column densities. The HVCs toward PKS 2155–304 have accurate H I column density measurements. As a result, models of those HVCs are much better constrained. For the comparisons of models to observations, we adopt  $2\sigma$  error bars for the measured column densities. Allowing this flexibility in the comparisons is useful, given the simplicity of the models and the complexity of the actual situation. In addition, in cases where line profiles indicate the presence of saturation (C III and Si III for the  $-140 \text{ km s}^{-1}$  component toward PKS 2155–304; Si III for the  $-300 \text{ km s}^{-1}$  component toward Mrk 509), we adopt the measured value as a lower limit to the column density. The mean of the column densities obtained from the C IV doublet is used for the HVCs toward PKS 2155–304 since saturation is not present. We have considered three approaches for the ionization of these HVCs, which are discussed individually below.

#### 4.3.1. Photoionization by Galactic Starlight

The first approach we consider is that the HVCs are in the Galactic halo ( $d < 50 \text{ kpc}$ ) and photoionized by stars in the disk. For energetic reasons, UV photons from massive stars in the disk are thought to be responsible for ionizing a significant majority of the ionized gas in the Galaxy and low halo (Reynolds 1993). Some HVCs have been detected in H $\alpha$  (Tuftte et al. 2002), and the assumption of photoionization by stars in the disk is often used to constrain their distances (Bland-Hawthorn & Maloney 2002). In order to examine the measured column densities, we have generated a grid of photoionization models using the code CLOUDY (Ferland 1996). We make the simplifying assumption that the absorbing gas

can be treated as plane-parallel slabs illuminated by incident radiation dominated by OB associations. The models assume a Kurucz model atmosphere ( $T_{\text{eff}} = 35,000$  K) and include metallicity as a free parameter, although the relative abundance pattern is assumed to be solar. Studies of H $\alpha$  emission measures of various HVCs have been argued (Bland-Hawthorn & Putman 2001; Weiner, Vogel, & Williams 2002) to be consistent with radiation from our Galaxy at the level of  $\log \phi \approx 5.5$  (photons  $\text{cm}^{-2} \text{s}^{-1}$ ), where  $\phi$  is the normally incident ionizing photon flux. Since the intensity of the field is fixed, we run models for a range of different ionization parameter,  $U$ , by varying the hydrogen number density within the cloud ( $U \propto \phi/n_{\text{H}}$ ).

The CLOUDY models generated using a stellar ionizing spectrum are generally successful at predicting the measured column densities of the singly ionized and neutral species. We find three generic failures of these photoionization models: (1) All species doubly ionized and higher are underpredicted by models in which the low-ionization species are used to constrain the field; (2) For any reasonable value of the ionization parameter,  $U$ , the stellar photoionization models produce very low ionization fractions of C IV relative to C II; (3) These photoionization models are unable to produce the observed amount of O VI. Clearly, if the gas is photoionized, the radiation field must be harder than that produced by massive stars (the O V ionization potential is  $\chi_{\text{OV}} = 113.87$  eV or 8.4 ryd).

#### 4.3.2. Photoionization by Extragalactic Background

Since a hard spectrum ionizing source is required to explain the ionization pattern in these HVCs, a likely source is the integrated radiation from background QSOs and AGN. This approach assumes, in effect, that the HVCs are at large distances from the Galactic plane ( $d > 100$  kpc) so that contributions from OB-star radiation escaping the galaxy are minimal (Giroux & Shull 1997). We use the same CLOUDY method as above, though we adopt a typical extragalactic radiation field with  $\log \phi = 4.0$  (photons  $\text{cm}^{-2} \text{s}^{-1}$ ) and a power-law spectrum with a spectral index of  $\alpha = -1.8$  (Zheng et al. 1997; Telfer et al. 2002).

However, we find that single-parameter photoionization models cannot reproduce the HVC ionization pattern. For the stronger HVC components, we observe  $N(\text{C II}) \sim N(\text{C III}) \sim N(\text{C IV}) \sim N(\text{O VI})$ , within a factor of 3. No model with our prescribed AGN radiation field can simultaneously predict such an ionization pattern. If we constrain the models by  $N(\text{C II}) \sim N(\text{C IV})$ , then  $N(\text{O VI})$  is underpredicted by several orders of magnitude. When  $N(\text{C II}) \sim N(\text{O VI})$  is assumed, then  $N(\text{C IV})$  and  $N(\text{N V})$  are overpredicted by at least an order of magnitude. Although the weaker HVC components do not have measurable amounts of low-ionization species, the ionization pattern is still inconsistent with an extragalactic

QSO field characterized by a single value of  $U$ . Telfer et al. (2002) show that quasar spectral indices in the ionizing EUV (1–3 ryd) can vary widely, from  $\alpha = 0$  to  $-3$ . In some cases, the spectrum can be considerably harder than our adopted  $\alpha = -1.8$  ionizing spectrum. We explored the possibility of a harder field by adopting  $\alpha = -0.5$ , which was also inadequate in replicating the observations. Although such a spectrum is able to produce more O VI (8.4 ryd radiation), it does so at the expense of lower ions which are still observed at high column density. Additionally, we have explored models incorporating an extragalactic X-ray background. Although such a radiation field produces a larger O VI column density by a factor of 3 – 5, it is insufficient to reproduce the observations.

Though they did not observe O VI, S99 were able to explain simultaneously all the observed column densities within their  $2\sigma$  error bars by adopting a similar QSO-type field. However, their models predict values of  $N(\text{O VI})$  significantly lower than we observe, suggesting that O VI may be predominantly collisionally ionized. Since these models clearly have difficulty explaining the measured O VI columns, we next consider models which fit the set of column densities for species ionized to N V and below, as per S99. We consider the species ionized below O VI as arising from photoionization by the extragalactic background, while the O VI arises from collisional ionization.

In Figures 9 and 10, we plot the predicted column densities versus ionization parameter from the models of the  $-140 \text{ km s}^{-1}$  and  $-270 \text{ km s}^{-1}$  components, respectively, toward PKS 2155–304. The solid lines connecting the model data points define the  $2\sigma$  error bars of the column density measurements. Neutral species are not plotted, since their upper limits do not provide useful constraints on the field. Except for O VI, the observed column densities can be simultaneously fitted by a QSO-type extragalactic field. The ionization parameters of the models fitting the  $-140 \text{ km s}^{-1}$  and  $-270 \text{ km s}^{-1}$  components are  $\log U = -3.02$  ( $n_{\text{H}} = 3.5 \times 10^{-4} \text{ cm}^{-3}$ ) and  $\log U = -1.98$  ( $n_{\text{H}} = 3.2 \times 10^{-5} \text{ cm}^{-3}$ ), respectively. The H I column densities of the Mrk 509 HVC components are not well constrained, although adequate fits to species ionized below O VI can be obtained with similar metallicities, H I column densities, and ionization parameters. The fitted models for all four HVC components in the PKS 2155–304 and Mrk 509 sight lines, however, underpredict  $N(\text{O VI})$  by as much as several orders of magnitude. In § 4.3.3 we explore models in which the O VI column densities arise from collisional ionization.

As noted by S99, there are scaling laws that apply for optically thin clouds ( $\log N(\text{H I}) < 17.2$ ) with sub-solar metallicities. The most important of these scaling laws is the column density relation for species X,  $N(\text{X}) \propto Z_{\text{X}} N(\text{H I})$ , where  $Z_{\text{X}}$  is the metallicity of element X. Therefore, models with the same value of  $Z_{\text{X}} N(\text{H I})$  predict essentially the same runs of column density versus  $U$ . The HVC components toward PKS 2155–304 have well-constrained

H I column densities. Since the fits to the observations are valid over a fairly narrow range in  $U$ , the metallicity and other properties can then be constrained by the uncertainty in  $N(\text{H I})$  and the use of the column density scaling law. In accordance with that scaling law, we have performed model calculations for the PKS 2155–304 HVC components over the range of uncertainty in  $N(\text{H I})$ . Since only weak upper limits,  $\log N(\text{H I}) < 17.69$ , can be derived for the HVCs toward Mrk 509, the parameter space of photoionization models is not well constrained. Therefore, we restrict the following discussion on cloud properties and physical conditions to the PKS 2155–304 sight line.

We obtain metallicities for the  $-140 \text{ km s}^{-1}$  and  $-270 \text{ km s}^{-1}$  components toward PKS 2155–304 of  $\log Z_{140} = -0.47^{+0.15}_{-0.24}$  and  $\log Z_{270} = -1.20^{+0.28}_{-0.45}$ , respectively, similar to those in HVC Complex C (CSG). For the photoionized component of the HVCs, we can compute the pressure,  $P/k = 2.3n_{\text{H}}T$  (assuming a fully ionized gas with  $\text{He}/\text{H} = 0.1$ ), and the cloud size,  $D \propto N_{\text{H}}/n_{\text{H}}$ . A summary of the properties obtained from the models is shown in Table 6. Shown for each component are three models using H I columns constrained by the observations. The inferred pressures,  $P/k \sim 1 - 10 \text{ K cm}^{-3}$ , are somewhat low, consistent with the S99 results for the HVCs toward Mrk 509. Such a pressure is significantly below the expected coronal gas pressure,  $P/k \gtrsim 100 \text{ K cm}^{-3}$ , in the Galactic halo. Assuming that the HVCs are in pressure equilibrium would imply distances well beyond the Galactic halo. The inferred size,  $D \sim N_{\text{H}}/n_{\text{H}}$ , of the  $-270 \text{ km s}^{-1}$  component,  $D_{270} = 54^{+86}_{-24} \text{ kpc}$ , is an order of magnitude larger than that of the  $-140 \text{ km s}^{-1}$  component,  $D_{140} = 4.0^{+2.9}_{-1.4} \text{ kpc}$ . This fact suggests an intergalactic location for the  $-270 \text{ km s}^{-1}$  HVC.

However, we note that the ionization parameter, and thus the gas pressure, in these models is constrained primarily by the observed C IV and Si IV column densities. To explore the role of high-velocity C IV and Si IV detections on photoionization modeling, we have considered CLOUDY models of Complex C along the sight line toward PG 1259+593, irradiated by the same QSO-type field with  $\alpha = -1.8$ . Complex C is a large ensemble of HVCs believed to be falling into the Galaxy from the low halo (Wakker et al. 1999; CSG). However, significant columns of Si IV, C IV, and O VI associated with Complex C are detected in this sight line. As stated in the previous section, a radiation field arising from Galactic starlight cannot produce significant columns of C IV and Si IV. If we constrain the ionization parameter of a QSO-type field by the C IV and Si IV columns observed towards PG 1259+593, we obtain the same low densities and low pressures as those found in the models for the PKS 2155–304 HVCs. However, the observed column densities,  $\log N(\text{H I}) \approx 19 - 20$ , and transverse sizes, 100-300 pc, for the Complex-C gas (CSG) suggest  $n_{\text{H}} \sim 0.01 - 0.1 \text{ cm}^{-3}$ , in contradiction to the low densities needed to achieve a high  $U$  parameter. The models in CSG (Figure 16) also suggest such a density. Similar densities are obtained by Wakker et al. (1999), who find that  $n_{\text{H}} \sim 0.05 - 0.1 \text{ cm}^{-3}$  for Complex C, based on a

5 – 25 kpc range of possible distance.

Therefore, we find that the PKS 2155–304 HVCs have similar physical conditions to those in Complex C, but at much lower  $N(\text{H I})$ . Since Complex C is a Galactic halo object, it is not unreasonable to assume that the PKS 2155–304 HVCs are as well. We further suggest that neither the physics of the highly ionized gas nor its connection to the neutral and low ionization gas are adequately understood.

#### 4.3.3. Contributions from Collisional Ionization

We believe that the strong O VI absorption in these ionized HVCs requires a significant contribution from collisional ionization. As demonstrated above, the observed column densities of species ionized below O VI in these HVCs can be explained by photoionization from an extragalactic background produced by QSOs and AGN. In the absence of an unusually hard ionizing field, gas at  $T \sim 10^{5.5 \pm 0.3}$  K is required to produce significant amounts of O VI. Such gas probably arises in cooling layers, over a range of temperatures at  $T < 10^6$  K.

Although a single-temperature collisional model cannot explain all the observed column densities, it is often useful to explore the ionization ratios using ionization fractions for collisional ionization equilibrium at fixed  $T$  (CIE; Sutherland & Dopita 1993). We have therefore calculated the expected column densities based on  $N(\text{H I})$  in the collisionally ionized regions. Since it is primarily the O VI that is underpredicted by the extragalactic photoionization models, we take the approach of considering that it arises in a separate, collisionally ionized component. Such a component could manifest itself as a mixing boundary between the photoionized cloud core and the WHIM. With a solar abundance pattern, this absorber would produce virtually no low-ionization species, while producing 2 – 3 orders of magnitude lower C IV and N V column densities than O VI. (Gas that cools from  $10^6$  K to  $10^4$  K would produce additional C IV.) Assuming that the metallicities in the photoionized and collisionally ionized regions are equal, we can then use the measured values of  $N(\text{O VI})$  to calculate  $N(\text{H})$  and  $N(\text{H I})$  in the collisionally ionized regions. The contribution of photoionized gas to  $N(\text{H})$  is given by the photoionization models.

The  $N(\text{O VI})$  observations imply nearly as much  $10^{5.5}$  K collisionally ionized gas as photoionized gas, while contributing 2 to 4 orders of magnitude less in  $N(\text{H I})$  than the photoionized gas. To explain the observations, the  $-140 \text{ km s}^{-1}$  component requires a factor of 3 less collisionally ionized than photoionized gas, although the  $-270 \text{ km s}^{-1}$  component would have nearly equal amounts of each. However, if the collisionally ionized component is in pressure equilibrium with the photoionized component, then the implied size of the colli-

sionally ionized component is more than an order of magnitude larger than the photoionized component. Reflecting on the photoionized cloud sizes in Table 6, we believe this model is unreasonable. One possible way of explaining this discrepancy would be if the collisionally ionized component was sufficiently dense to allow radiative cooling. The cooling time of low-density hot gas is approximately

$$t_{\text{cool}} = \frac{1.5kT}{n_H\Lambda(T)} \approx \frac{(2.1 \text{ Gyr})T_6}{n_{-4}\Lambda_{-22.5}}, \quad (3)$$

where  $n_{-4} = n_H/(10^{-4} \text{ cm}^{-3})$  and  $T_6 = (T/10^6 \text{ K})$ . Here,  $\Lambda_{-22.5}$  is the radiative cooling rate coefficient in units of  $10^{-22.5} \text{ erg cm}^3 \text{ s}^{-1}$ , typical of gas at  $10^6 \text{ K}$  with  $0.1 - 0.3$  solar metallicity (Sutherland & Dopita 1993). At low densities, these cooling layers may be out of ionization equilibrium. Some or all of the observed C IV and Si IV could be attributed to the collisionally ionized component, thus allowing for lower ionization parameters and smaller cloud sizes. The possible multi-component structure seen in Figure 2 for the  $-140 \text{ km s}^{-1}$  component towards PKS 2155–304, is suggestive of such an association between the C IV, Si IV, O VI, and possibly the doubly ionized components. Indebetouw & Shull (2003) summarize the predictions of a variety of theoretical models of interactions between gas in two thermal phases, such as evaporating cloudlets (Ballet et al. 1986), planar conduction fronts (Borkowski et al. 1990), stellar wind and supernovae bubbles (Slavin & Cox 1993), turbulent mixing layers (Slavin, Shull, & Begelman 1993), and more generic cooling flows.

A specific scenario consistent with the ionization and kinematic features of the O VI is the “infalling clump” model. In this picture, the HVCs represent clumps of gas, falling into the Galactic halo after large distances or returning to the disk from injection into a Galactic fountain. (The metallicity of the gas would be a distinguishing feature for these two scenarios.) Interactions between the clump and the gaseous substrate of the low halo would produce a bow shock, and the refraction and shear of the post-shock gas will create a range of observed radial velocities, of order  $(1 - 2)V_s \sin b$ , if the HVC is falling directly toward the plane at Galactic latitude  $b$  and velocity  $V_s$ . Such velocity shear has been seen in the bow shocks toward many Herbig-Haro objects (Hartigan, Raymond, & Hartmann 1987), and may be reflected in the broad ( $\sim 100 \text{ km s}^{-1}$ ) profiles of O VI.

We can also consider more generic predictions of the C IV and Si IV which may be associated with these nonequilibrium physical states. In general, substantially more C IV and Si IV may co-exist with the O VI than would be inferred from collisional ionization equilibrium. While the fractions of  $N(\text{C IV})/N(\text{O VI})$  and  $N(\text{Si IV})/N(\text{O VI})$  are ultimately dependent on the details of the specific model, a representative range in these fractions is  $N(\text{C IV})/N(\text{O VI}) \approx 0.1 - 0.2$  and  $N(\text{Si IV})/N(\text{O VI}) \lesssim 0.01$ . If we associate 10-20% of our measured column densities of  $N(\text{C IV})$  and  $N(\text{Si IV})$  with this hot gas, this is not enough to change the inferred physical properties of the photoionized gas substantially.



We can make a substantial change in the acceptable ionization parameter for the photoionized gas, and thus in the inferred density, if nearly all the multiply ionized species (O VI, C III, C IV, Si III, Si IV, N V) are associated with collisionally ionized gas. If the radiation field from the CLOUDY models is then constrained by H I and singly-ionized species, significantly lower photoionization parameters are possible. As a result, the  $-140 \text{ km s}^{-1}$  component could have a gas density as much as six times larger than the values listed in Table 6, and the gas density of the  $-270 \text{ km s}^{-1}$  component could be larger by an even greater factor. In such a scenario, a larger gas pressure would make an association with the Galaxy more likely for these HVCs.

#### 4.3.4. Possible contributions from the WHIM

X-ray absorption lines of O VII and O VIII are detected at  $z = 0$  in the PKS 2155–304 sight line, both with *Chandra* (Nicastro et al. 2002) and XMM (Rasmussen, Kahn, & Paerels 2003). In this section we consider the implications of these detections on the characteristics of the absorbing gas. Since the velocity resolution of the X-ray data is inferior to that of the UV data by a factor of  $\sim 30$ , the O VII and O VIII features cannot be conclusively associated with the high-velocity UV lines. Since O VI components at  $z = 0$  are detected in this sight line, both at high velocity and Galactic LSR velocity, it is likely that the X-ray absorption features also have multi-component structure, albeit unresolved. Nevertheless, we consider the scenario where the entire O VII and O VIII absorption arises in a single component at high-velocity.

We adopt  $\log[N(\text{O VIII})/N(\text{O VII})] = 0.12_{-0.69}^{+0.34}$  based on the column densities reported in Nicastro et al. (2002). This corresponds to a temperature of  $\log T = 6.30 \pm 0.15$ , assuming collisional ionization equilibrium (Sutherland & Dopita 1993). The O VI to O VII ionization ratio in CIE would then be  $\log[f(\text{O VI})/f(\text{O VII})] = -2.3$ . Therefore, if the entire O VII/O VIII absorption occurs in a WHIM component at the same velocity as the high-velocity UV absorption, with  $N(\text{O VII}) = 4.0 \times 10^{15} \text{ cm}^{-2}$ , then the WHIM could account for a column density,  $N(\text{O VI}) = 2.0 \times 10^{13} \text{ cm}^{-2}$ . Since some of the O VII/VIII absorption could be attributed to a Galactic component at  $V_{\text{LSR}} \approx 0 \text{ km s}^{-1}$ , we stress that this value is an upper limit to the amount of O VI that would exist in the high-velocity WHIM. In the two high-velocity components towards PKS 2155–304, we measure a total column density of  $N(\text{O VI}) = 1.0 \times 10^{14} \text{ cm}^{-2}$ , a factor of five larger than could be accounted for by a velocity-coincident WHIM absorber. It is also of note that the O VI absorption is confined to a velocity range of half-width  $\sim 100 \text{ km s}^{-1}$ , whereas the shocked WHIM is expected to extend over a broader region, at distances of  $2 - 25h^{-1} \text{ Mpc}$ , or at  $V_{\text{LSR}} = 200 - 2500 \text{ km}$

$s^{-1}$  (Kravtsov, Klypin, & Hoffman 2002). We therefore conclude that most of the O VI gas is present in the high-velocity cloud traced by C II/III/IV and Si II/III/IV. We emphasize that this does not rule out the possibility that the O VII/VIII absorber may trace a WHIM filament, or that some of the O VI absorption arises in the WHIM.

## 5. CONCLUSIONS

Using *FUSE* and *HST*/STIS data for the targets PKS 2155–304 and Mrk 509, we have investigated the “highly ionized high-velocity clouds” in those sight lines. We measured column densities of species associated with the HVCs, as well as the H I column density of the HVCs toward PKS 2155–304 using Lyman-series absorption. Using these results, we have come to the following conclusions:

**(1) Highly Ionized HVCs.** With *HST* and *FUSE*, we have studied four “highly ionized” HVCs proposed by S99, observing H I and multiple ion stages of carbon, silicon, and O VI. We confirm the ionized nature of three of the four HVCs, the exception being the HVC at  $-140 \text{ km s}^{-1}$  toward PKS 2155–304, which has many low ions (H I, C II, Si II). A core-halo effect is apparent with high-ionization species (doubly-ionized and above) which show a larger extent in velocity space than the low-ionization species. Such behavior may indicate a difference in physical origin between the high- and low-ionization gas.

**(2) Multiphase Gas.** We observe far more O VI in these HVCs than is consistent with photoionization models; we believe O VI is collisionally ionized. The HVCs exhibit absorption ranging from H I to C IV, Si IV, and O VI, suggesting that the clouds are multiphase. The combination of hot collisionally ionized gas with warm photoionized gas complicates the interpretation. We propose that the high ions arise from hot gas, possibly produced behind bowshocks from clumps falling toward the Galactic plane. Velocity shear behind these bowshocks is consistent with the observed broad ( $\sim 100 \text{ km s}^{-1}$ ) O VI absorption profiles.

**(3) Column Density Ratios.** Some of the ion ratios in these HVCs differ from most Galactic halo gas. The ionization pattern in the stronger HVC components has  $N(\text{C II}) \sim N(\text{C III}) \sim N(\text{C IV}) \sim N(\text{O VI})$  within a factor of 3. Some of these ratios are similar to intergalactic gas, both the high- $z$  Ly $\alpha$  forest and a low- $z$  absorber associated with the Virgo cluster. However, the presence of low ions indicates that the density is significantly higher than that expected for the WHIM. This implies, at least for the HVCs towards PKS 2155–304 and Mrk 509, that the high-velocity O VI do not necessarily trace the WHIM, as proposed by Nicastro et al. (2002, 2003), but instead may trace HVCs with low total hydrogen column density. Some C IV and Si IV could arise from thermal instability in

cooling WHIM gas, but this may be inconsistent with the broad O VI velocity profiles.

**(4) Photoionization models.** Single-parameter ( $U$ ) models cannot reproduce all the observed column densities. If O VI is assumed to be collisionally ionized, a QSO-type radiation field can reproduce the other species' column density pattern. In this case, the radiation field is constrained by C IV and Si IV, which imply low gas pressures, large cloud sizes, and an extragalactic location for the HVCs. However, models of the PG 1259+593 sight line toward HVC Complex C (thought to have  $n_H \sim 0.01 - 0.1 \text{ cm}^{-3}$ ) yield the same, erroneously low gas pressures when the field is constrained by the high-ion measurements. This fact indicates that the physics of hot gas at cloud interfaces may not be well understood.

**(5) HVC Gas Pressures.** Simple cooling layers, from  $10^6$  K down to  $10^4$  K, cannot account for the C IV and Si IV measurements, given the strong absorption in O VI. A substantial decrease in the ionization parameter,  $U$ , and increase in the gas pressure,  $P/k$ , is possible in a multiphase model in which species doubly-ionized and above arise from collisional ionization. If photo-ionization models are then constrained by H I and the singly-ionized species, significantly larger gas pressures are allowed, and a Galactic association for the HVCs is possible.

This work was supported by grant GO-08571.01-A (HST Cycle 8) from the Space Telescope Science Institute and NAG5-7262 from NASA/LTSA. The FUSE data were obtained by the Guaranteed Time Team for the NASA-CNES-CSA mission operated by the Johns Hopkins University. Financial support to U.S. participants was provided by NASA contract NAS5-32985. We thank Ken Sembach and Blair Savage for helpful discussions on Galactic halo gas and HVCs. We also thank the referee, Fabrizio Nicastro, for useful comments on the final preparation of this paper.

## REFERENCES

- Ballet, J., Arnaud, M., & Rothenflug, R. 1986, *A&A*, 161, 12
- Bland-Hawthorn, J., Maloney, P. R. 2002, in *ASP Conf. Ser. 254, H $\alpha$  Distance Constraints for High Velocity Clouds in the Galactic Halo*, ed. J. S. Mulchaey & J. Stocke (San Francisco: ASP), 267
- Bland-Hawthorn, J., & Putman, M. E. 2001, in *ASP Conf. Ser. 240, Gas and Galaxy Evolution*, ed. J. E. Hibbard, M. Rupen, & J. H. van Gorkom (San Francisco: ASP), 369
- Blitz, L., Spergel, D. N., Teuben, P. J., Hartmann, D., & Burton, W. B. 1999, *ApJ*, 514, 818

- Borkowski, K. J., Balbus, S. A., & Fristrom, C. C. 1990, *ApJ*, 355, 501
- Braun, R., & Burton, W. B. 1999, *A&A*, 341, 437
- Bregman, J. N. 1980, *ApJ*, 236, 577
- Collins, J. A., Shull, J. M., & Giroux, M. L. 2003, *ApJ*, 585, 336 (CSG)
- Fang, T, Marshall, H. L., Lee, J. C., Davis, D. S., & Canizares, C. R. 2002, *ApJ*, 572, L127
- Ferland, G. J. 1996, HAZY, A Brief Introduction to CLOUDY (Univ. Kentucky Dept. Astron. Internal Rep.)
- Flynn, C., & Morell, O. 1997, *MNRAS*, 286, 617
- Fox, A. J., Savage, B. D., Wakker, B. P., Richter, P., Sembach, K. R., & Tripp, T. M. 2004, *ApJ*, in press
- Giroux, M. L., & Shull, J. M. 1997, *AJ*, 113, 1505
- Hartigan, P. Raymond, J., & Hartmann, L. 1987, *ApJ*, 316, 323
- Heckman, T. M., Norman, C. A., Strickland, D. K., & Sembach, K. R. 2002, *ApJ*, 577, 691
- Holweger, H. 2001, in *AIP Conf. Ser.* 598, *Solar and Galactic Composition*, ed. R. F. Wimmer-Schweingruber (New York: Springer), 23
- Hopp, U., Schulte-Ladbeck, R. E., & Kerp, J. 2003, *MNRAS*, 339, 33
- Indebetouw, R., & Shull, J. M. 2004, *ApJ*, in press
- Kraemer, S. B., et al. 2003, *ApJ*, 582, 125
- Kravtsov, A. V., Klypin, A., & Hoffman, Y. 2002, *ApJ*, 571, 563
- Maloney, P. R., & Putman, M. E. 2003, *ApJ*, 589, 270
- Mathur, S., Weinberg, D. H., & Chen, X. 2003, *ApJ*, 582, 82
- Moos, H. W. 2000, *ApJ*, 538, L1
- Nicastro, F., et al. 2002, *ApJ*, 573, 157
- Nicastro, F., et al. 2003, *Nature*, 421, 719
- Putman, M. E., Bland-Hawthorn, J., Veilleux, S., Gibson, B. K., Freeman, K. C., & Maloney, P. R. 2003, *ApJ*, 597, 948
- Rasmussen, A., Kahn, S. M., & Paerels, F. 2003, in *The IGM/Galaxy Connection*, (Dordrecht: Kluwer Publ.), ed. J. Rosenberg & M. Putman, 109
- Reynolds, R. J. 1993, in *AIP Conf. Proc.* 278, *Back to the Galaxy*, ed. S. S. Holt & F. Verter (New York: AIP), 156
- Richter, P., et al. 2001, *ApJ*, 559, 318

- Savage, B. D., & Sembach, K. R. 1991, *ApJ*, 379, 245
- Sembach, K. R., et al. 2003, *ApJS*, 146, 165
- Sembach, K. R., & Savage, B. D. 1992, *ApJS*, 83, 147
- Sembach, K. R., Savage, B. D., Lu, L., & Murphy, E. M. 1995, *ApJ*, 451, 616
- Sembach, K. R., Savage, B. D., & Tripp, T. M. 1997, *ApJ*, 480, 216
- Sembach, K. R., Savage, B. D., Lu, L., & Murphy, E. M. 1999, *ApJ*, 515, 108 (S99)
- Shapiro, P. R., & Field, G. B. 1976, *ApJ*, 205, 762
- Shull, J. M., Tumlinson, J., & Giroux, M. L. 2003, *ApJ*, 594, L107
- Simon, J. D., & Blitz, L. 2002, *ApJ*, 574, 726
- Slavin, J. D., & Cox, D. P. 1993, *ApJ*, 417, 187
- Slavin, J. D., Shull, J. M., & Begelman, M. C. 1993, *ApJ*, 407, 83
- Songaila, A., & Cowie, L. L. 1996, *AJ*, 112, 335 (SC)
- Sutherland, R. S., & Dopita, M. A. 1993, *ApJS*, 88, 253
- Telfer, R. C., Zheng, W., Kriss, G. A., & Davidsen, A. F. 2002, *ApJ*, 565, 773
- Tripp, T. M., et al. 2002, *ApJ*, 575, 697
- Tripp, T. M., et al. 2003, *AJ*, 125, 3122
- Tufte, S. L., Wilson, J. D., Madsen, G. J., Haffner, L. M., Reynolds, R. J 2002, *ApJ*, 572, L153
- Wakker, B. P., et al. 1999, *Nature*, 402, 388
- Wakker, B. P., Kalberla, P. M. W., van Woerden, H., de Boer, K. S., & Putman, M. E. 2001, *ApJS*, 136, 537
- Wakker, B. P., & van Woerden, H. 1997, *ARA&A*, 35, 217
- Weiner, B. J., Vogel, S. N., & Williams, T. B. 2002, in *ASP Conf. Ser. 254, Extragalactic Gas at Low Redshift*, ed. J. S. Mulchaey & J. Stocke (San Francisco: ASP), 256
- Zheng, W., Kriss, G. A., Telfer, R. C., Grimes, J. P., & Davidsen, A. F. 1997, *ApJ*, 475, 469
- Zwaan, M. A. 2001, *MNRAS*, 325, 1142

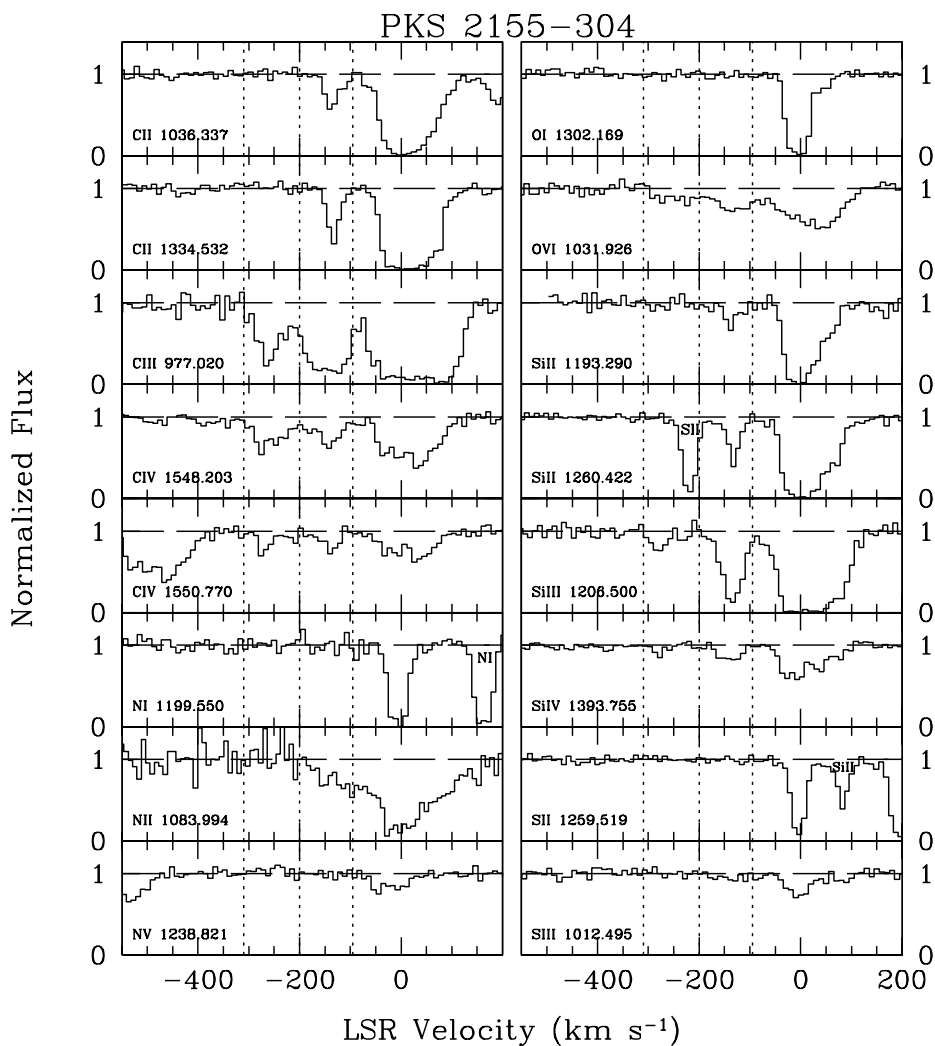


Fig. 1.— Normalized absorption profiles from STIS and *FUSE* data for PKS 2155–304. The vertical dashed lines indicate the integration ranges of the  $-140 \text{ km s}^{-1}$  ( $-200$  to  $-95 \text{ km s}^{-1}$ ) and the  $-270 \text{ km s}^{-1}$  ( $-310$  to  $-200 \text{ km s}^{-1}$ ) components.

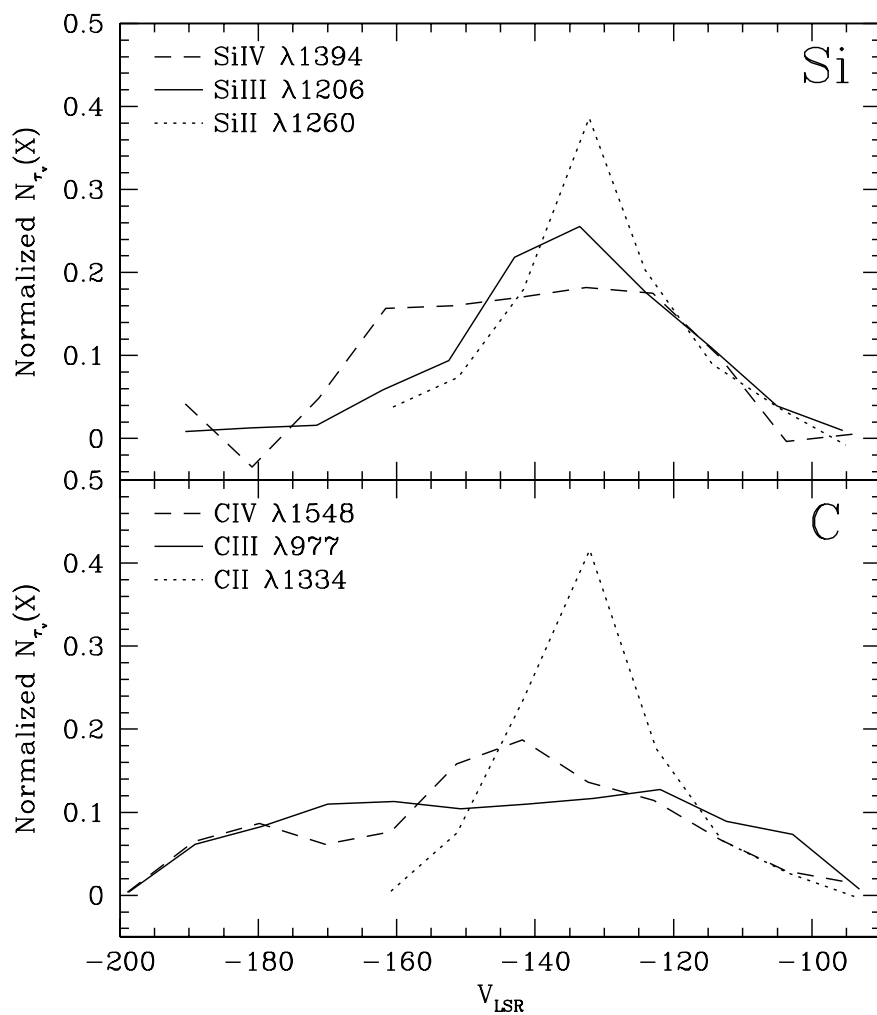


Fig. 2.— Normalized column density profiles of silicon (*top*) and carbon (*bottom*) for the  $-140 \text{ km s}^{-1}$  component in the PKS 2155–304 sight line. The more concentrated profile of the singly-ionized species indicates a possible core-halo structure of the HVC.

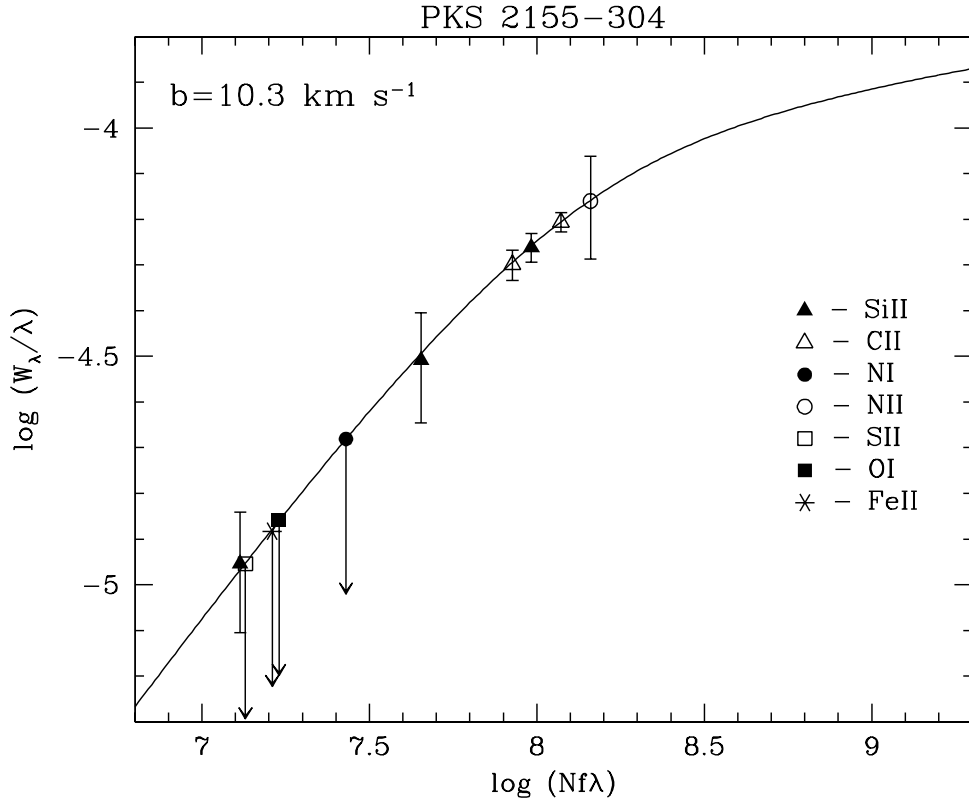


Fig. 3.— Empirical curve of growth for ions observed in the PKS 2155–304 sight line ( $-140 \text{ km s}^{-1}$  component). The Si II and C II lines are best fitted by a curve with  $b = 10.3_{-2.9}^{+6.5} \text{ km s}^{-1}$ .



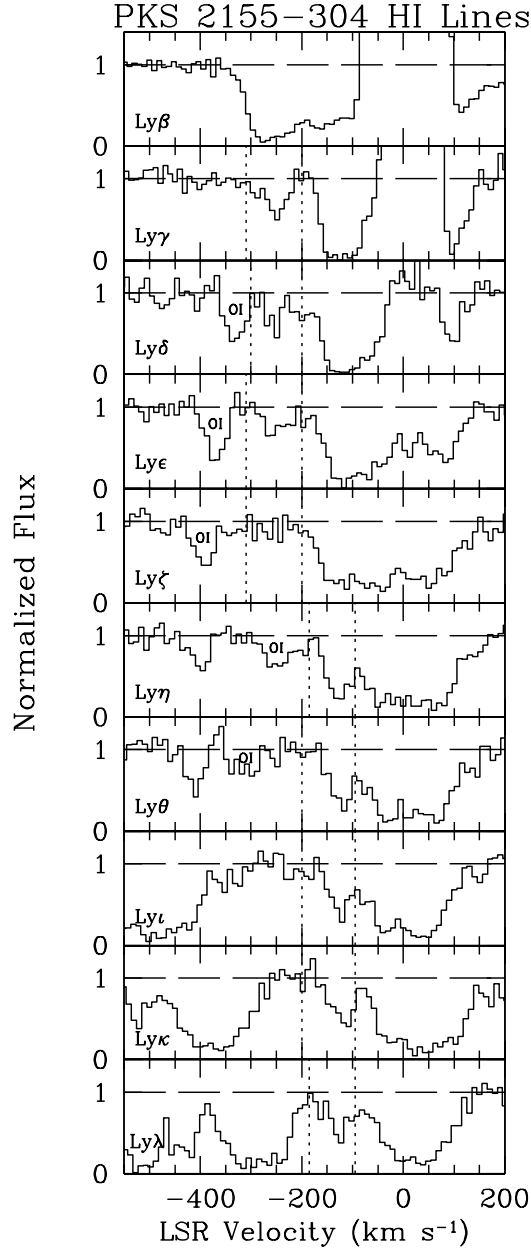


Fig. 4.— Normalized absorption profiles of H I Lyman lines from the PKS 2155–304 *FUSE* data. The vertical dashed lines indicate the Lyman lines for which the  $-140$  and  $-270$   $\text{km s}^{-1}$  components can be measured, as well as the adopted integration range. The  $-140$   $\text{km s}^{-1}$  component can be measured for Ly $\gamma$  through Ly $\zeta$ , while the  $-270$   $\text{km s}^{-1}$  can be measured for Ly $\eta$  through Ly $\lambda$ .

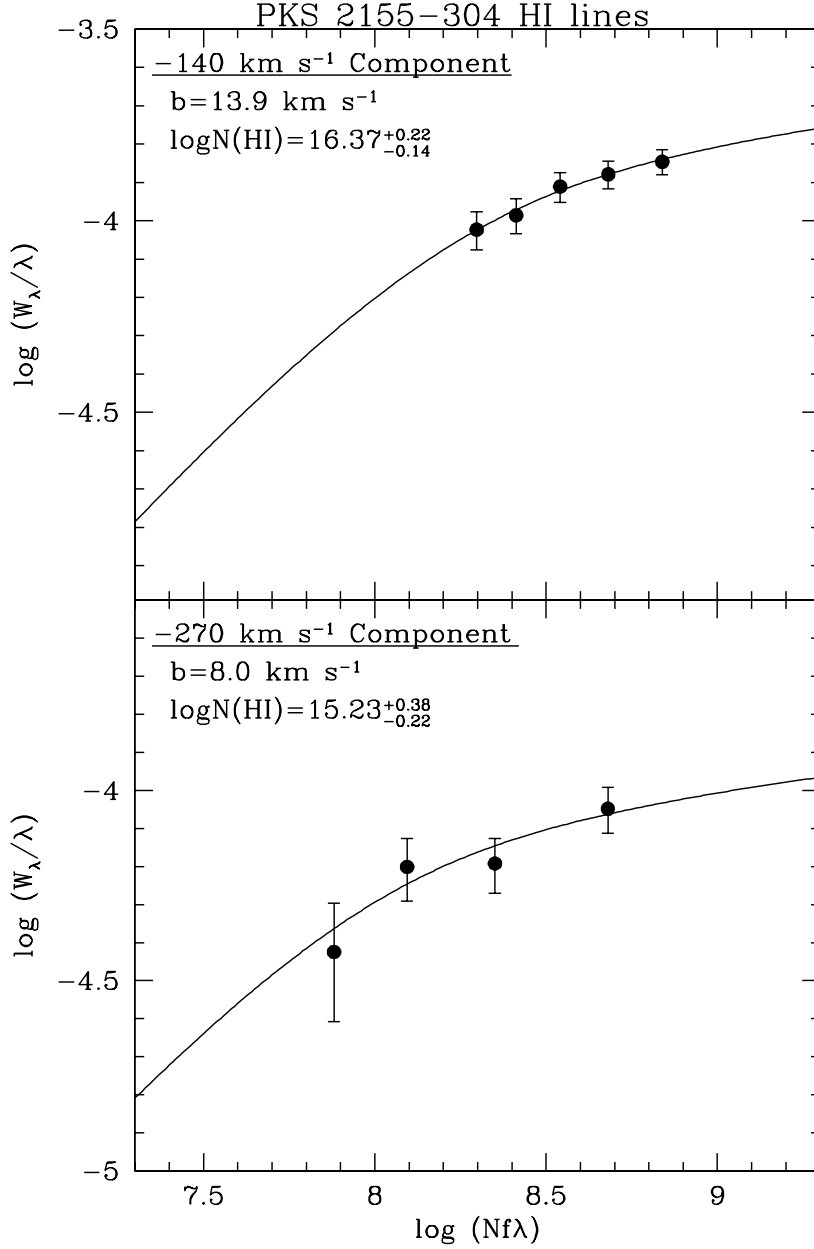


Fig. 5.— Empirical curves of growth for H I lines observed in the PKS 2155–304 sight line for the two high velocity components. The  $-140$  and  $-270 \text{ km s}^{-1}$  components are best fitted by curves with  $b = 13.9^{+3.1}_{-2.3}$  and  $b = 8.0^{+3.5}_{-2.0} \text{ km s}^{-1}$ , respectively. The measured column densities are, respectively,  $\log N(\text{H I}) = 16.37^{+0.22}_{-0.14}$  and  $\log N(\text{H I}) = 15.23^{+0.38}_{-0.22}$ .

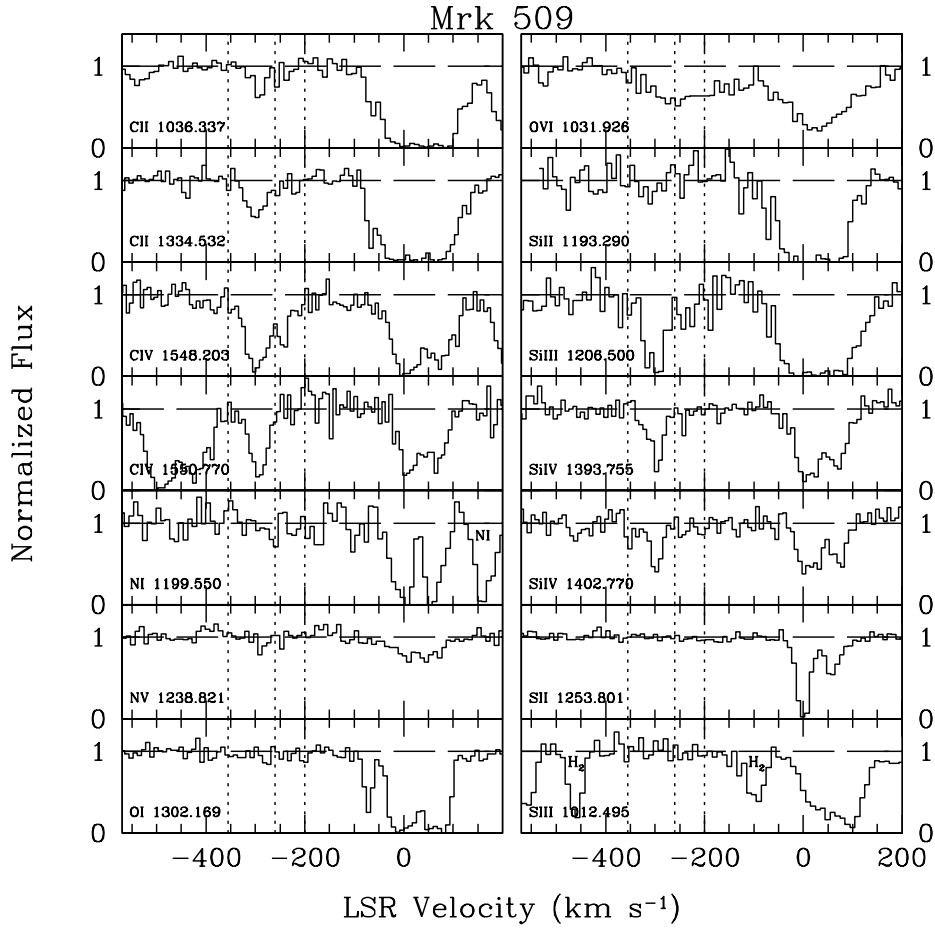


Fig. 6.— Normalized absorption profiles from STIS and *FUSE* data for Mrk 509. The vertical dashed lines indicate the integration ranges of the  $-240 \text{ km s}^{-1}$  ( $-260$  to  $-200 \text{ km s}^{-1}$ ) and the  $-300 \text{ km s}^{-1}$  ( $-355$  to  $-260 \text{ km s}^{-1}$ ) components.

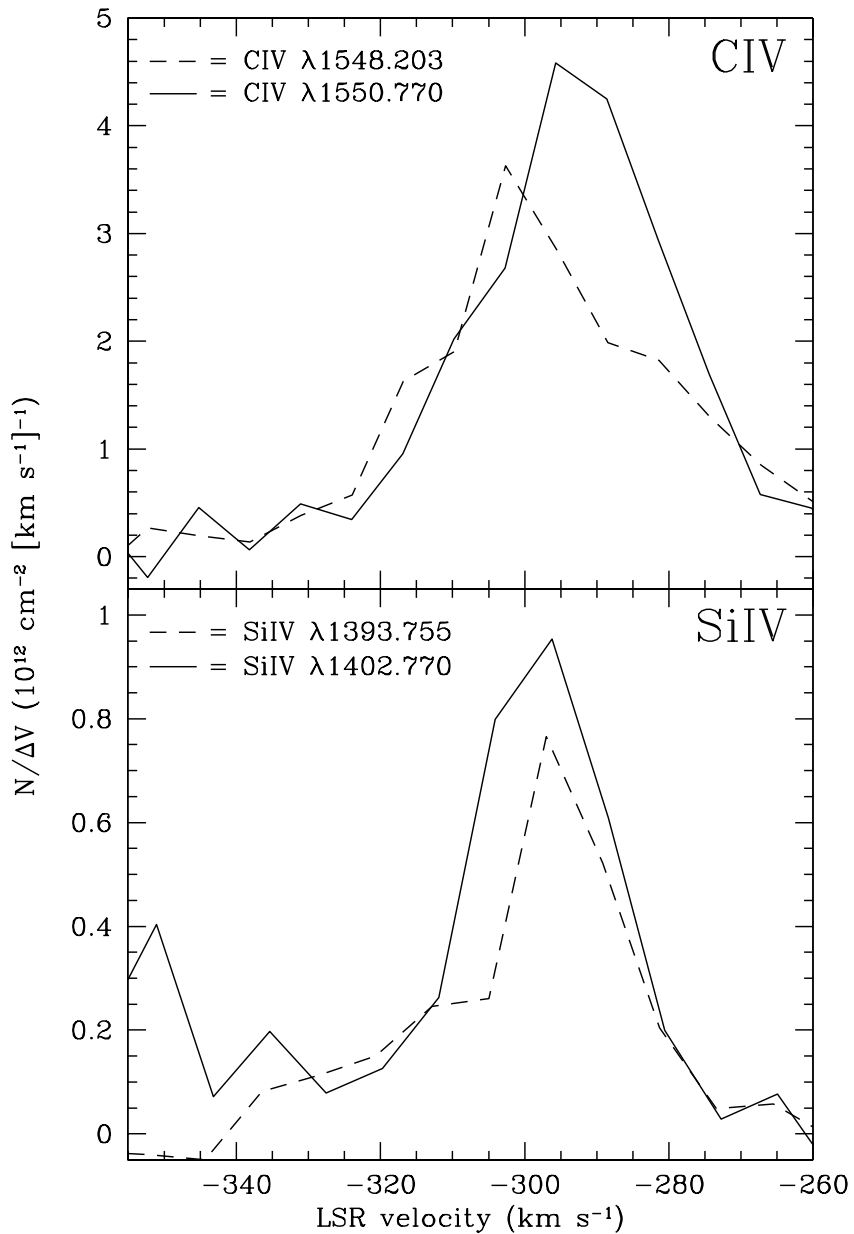


Fig. 7.— Column density profiles of C IV and Si IV for the  $-300 \text{ km s}^{-1}$  component in the Mrk 509 sight line. Plotted are the profiles from the strong (*dashed*) and weak (*solid*) lines in each doublet. The more peaked behavior of the profiles from the weak lines indicates the presence of saturation.

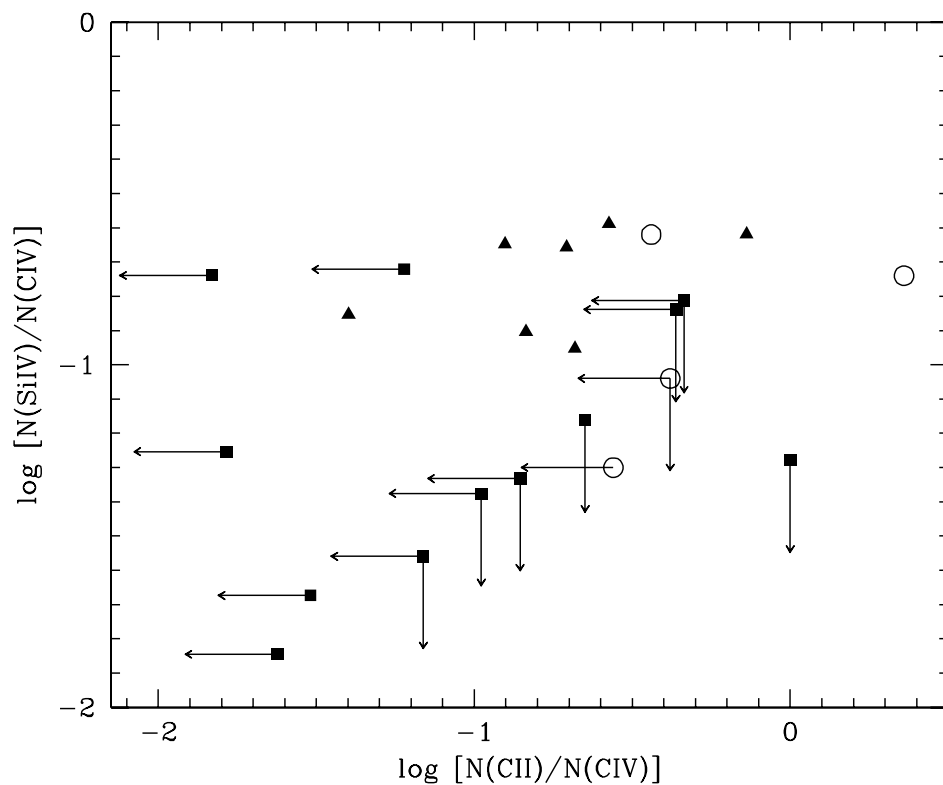


Fig. 8.— Diagnostic diagram of the ratios  $\log[N(\text{Si IV})/N(\text{C IV})]$  versus  $\log[N(\text{C II})/N(\text{C IV})]$  for  $z \sim 3$  Ly $\alpha$  forest clouds and the HVCs towards PKS 2155–304 and Mrk 509. Triangles are measurements and squares are limits from the Songaila & Cowie (1996) sample. The large open circles are for the HVCs towards PKS 2155–304 and Mrk 509. The data point with very high  $\log[N(\text{C II})/N(\text{C IV})]$  is for the  $-140 \text{ km s}^{-1}$  component toward PKS 2155–304.

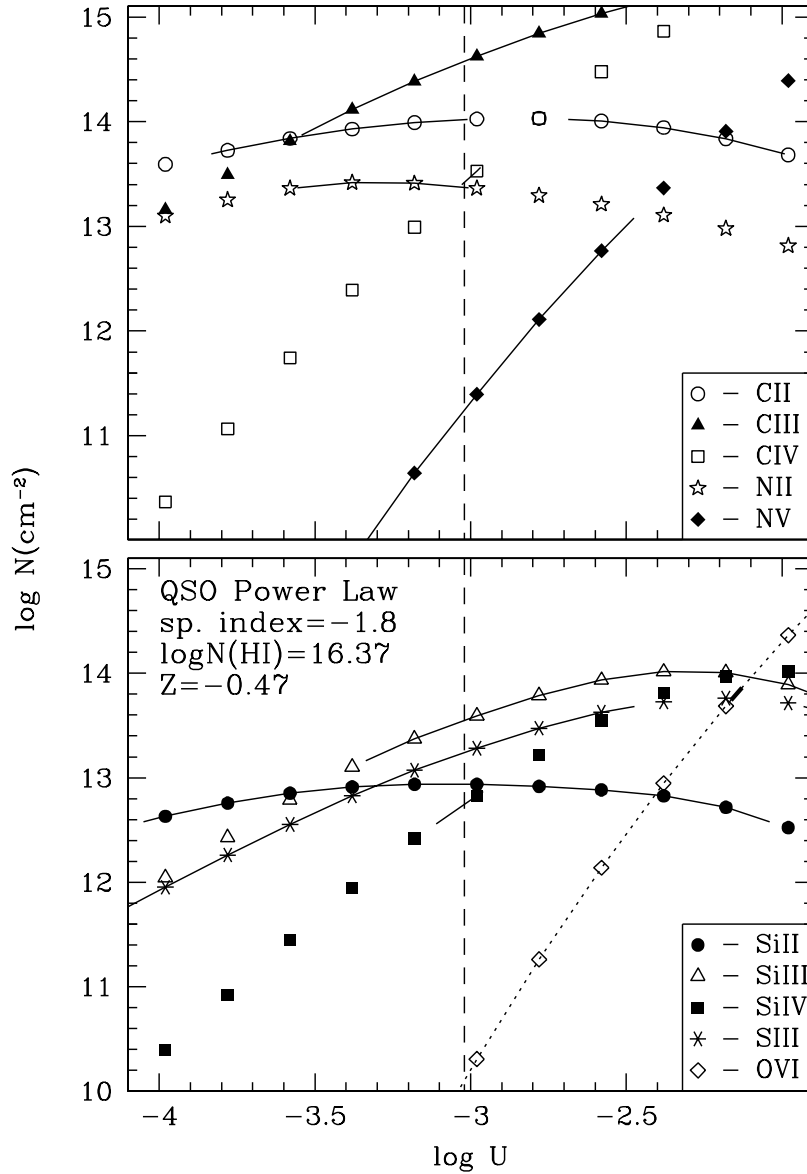


Fig. 9.— CLOUDY model calculations for the  $-140 \text{ km s}^{-1}$  HVC component toward PKS 2155–304. Plotted are the predicted column densities of various ion species versus  $\log U$  (points) and their constraints based on the observations (solid lines). Species are shown on two plots for clarity. For the constraints on the observed values, we use the  $2\sigma$  range of the measured value, the measured value as a lower limit if saturation is evident, or the upper limit on the measured value. The predicted run of  $N(\text{O VI})$  is indicated by the dotted line to emphasize the discrepancy between the predicted and observed values of  $N(\text{O VI})$ . The model shown is characterized by a QSO power law spectrum with  $\alpha = -1.8$ , an H I column density of  $\log N(\text{H I}) = 16.37$  and a metallicity of  $Z = 10^{-0.47} Z_{\odot}$ . The vertical dashed line indicates a value of ionization parameter,  $\log U = -3.02$ , which fits the observed column densities, excluding O VI.

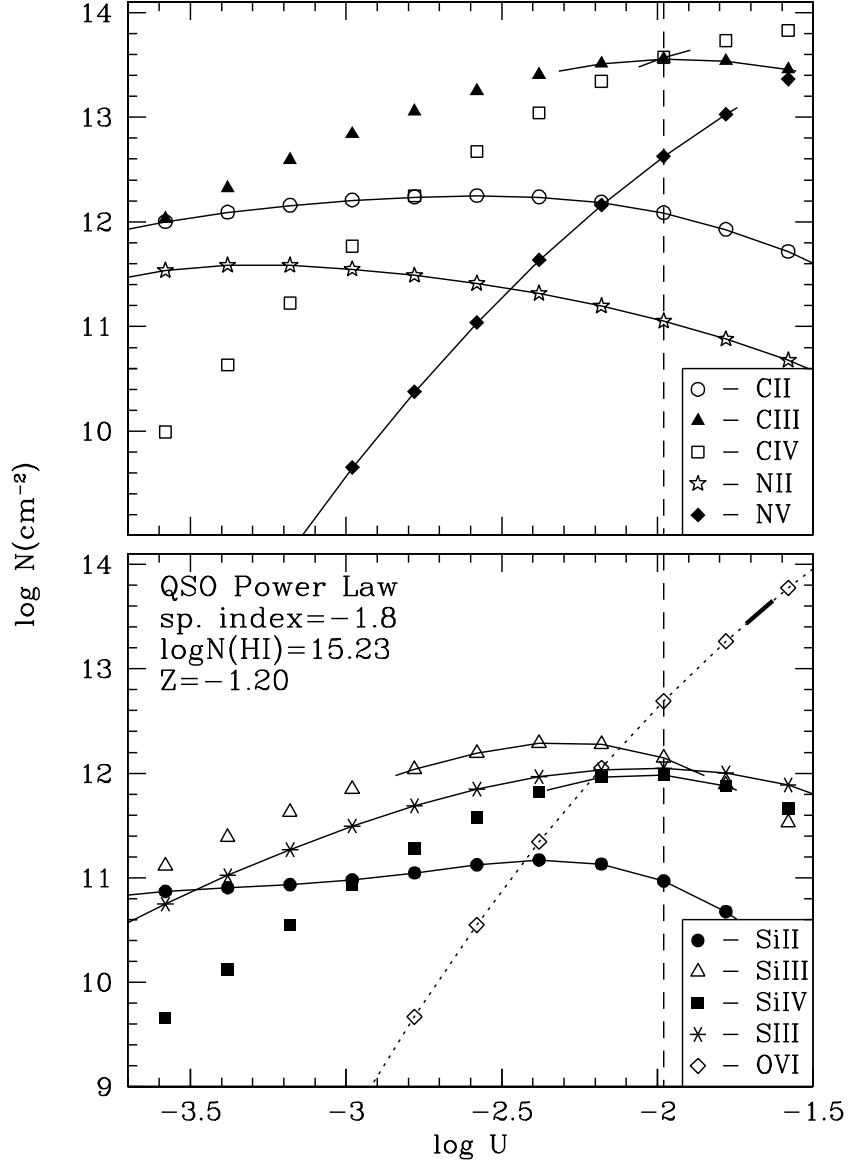


Fig. 10.— CLOUDY model calculations for the  $-270 \text{ km s}^{-1}$  HVC component toward PKS 2155–304. Plot symbols are the same as in Figure 8. The model shown is characterized by a QSO power law spectrum with  $\alpha = -1.8$ , an H I column density of  $\log N(\text{H I}) = 15.23$  and a metallicity of  $Z = 10^{-1.20} Z_{\odot}$ . The vertical dashed line indicates a value of ionization parameter,  $\log U = -1.98$ , which fits the observed column densities, excluding O VI.

Table 1. SUMMARY OF OBSERVATIONS

| Sightline    | Instrument               | Grating            | Program ID | Observation Date(s) | $T_{exp}$ (ks) | Number of Exposures |
|--------------|--------------------------|--------------------|------------|---------------------|----------------|---------------------|
| PKS 2155–304 | <i>HST-STIS</i>          | E140M <sup>a</sup> | 8125       | 1999 Nov; 2000 Sep  | 28.5           | 4                   |
|              | <i>FUSE</i> <sup>b</sup> | ...                | P108       | 1999 Oct; 2001 Jun  | 121.5          | 54                  |
| Mrk 509      | <i>HST-STIS</i>          | E140M              | 8877       | 2001 Apr            | 7.6            | 3                   |
|              | <i>FUSE</i>              | ...                | P108       | 2000 Sep            | 61.4           | 28                  |

<sup>a</sup>The STIS E140M provides wavelength coverage of 1150–1700 Å.

<sup>b</sup>The *FUSE* spectrum covers the wavelength range of 905–1187 Å.



Table 2. SUMMARY OF MEASUREMENTS: PKS 2155–304

| Species | $\lambda^a$<br>(Å) | $f^a$  | Component 1<br>$V_{LSR} = -140 \text{ km s}^{-1}$ |  | Component 2<br>$V_{LSR} = -270 \text{ km s}^{-1}$ |  |
|---------|--------------------|--------|---|--|---|--|
|         |                    |        | $W_\lambda$<br>(mÅ)                               | $\log N(X)^b$<br>( $N$ in $\text{cm}^{-2}$ ) | $W_\lambda$<br>(mÅ)                               | $\log N(X)^b$<br>( $N$ in $\text{cm}^{-2}$ ) |
| H I     | ...                | ...    | ...   | $16.37^{+0.22c}_{-0.14}$                     | ...   | $15.23^{+0.38c}_{-0.22}$                     |
| C II    | 1036.337           | 0.118  | $52 \pm 4$  | $13.84^{+0.10d}_{-0.07}$                     | $< 18$  | $< 13.21$                                    |
|         | 1334.532           | 0.128  | $83 \pm 4$  | ...  | $< 20$  | $< 13.00$                                    |
| C III   | 977.020            | 0.759  | $246 \pm 9$                                       | $13.87^{+0.02*}_{-0.02}$                     | $149 \pm 11$                                      | $13.52^{+0.03}_{-0.04}$                      |
| C IV    | 1548.203           | 0.190  | $112 \pm 10$                                      | $13.51^{+0.03}_{-0.04}$                      | $137 \pm 11$                                      | $13.60^{+0.04}_{-0.03}$                      |
|         | 1550.770           | 0.0948 | $51 \pm 9$  | $13.45^{+0.07}_{-0.08}$                      | $60 \pm 11$                                       | $13.52^{+0.07}_{-0.09}$                      |
| N I     | 1199.550           | 0.130  | $< 25$  | $< 13.24^d$                                  | $< 35$  | $< 13.32$                                    |
| N II    | 1083.994           | 0.115  | $75 \pm 19$                                       | $14.06^{+0.22d}_{-0.22}$                     | $< 62$  | $< 13.71$                                    |
| N V     | 1238.821           | 0.157  | $< 25$  | $< 13.08$                                    | $< 26$  | $< 13.09$                                    |
| O I     | 1302.169           | 0.0519 | $< 18$  | $< 13.40^d$                                  | $< 25$  | $< 13.51$                                    |
| O VI    | 1031.926           | 0.133  | $70 \pm 5$  | $13.80^{+0.03}_{-0.03}$                      | $42 \pm 5$  | $13.56^{+0.05}_{-0.06}$                      |
| Si II   | 1193.290           | 0.585  | $37 \pm 10$                                       | $12.81^{+0.12d}_{-0.10}$                     | $< 42$  | $< 12.77$                                    |
|         | 1260.422           | 1.184  | $69 \pm 5$  | ...  | ...   | ...  |
|         | 1526.707           | 0.132  | $17 \pm 5$  | ...  | $< 34$  | $< 13.10$                                    |
| Si III  | 1206.500           | 1.669  | $176 \pm 11$                                      | $13.16^{+0.02*}_{-0.02}$                     | $41 \pm 12$                                       | $12.33^{+0.10}_{-0.14}$                      |
| Si IV   | 1393.755           | 0.514  | $45 \pm 8$  | $12.74^{+0.07}_{-0.08}$                      | $15 \pm 5$  | $12.26^{+0.11}_{-0.16}$                      |
| S II    | 1259.519           | 0.0166 | $< 14$  | $< 13.81^d$                                  | $< 20$  | $< 13.94$                                    |
| S III   | 1012.495           | 0.0442 | $< 19$  | $< 13.68$                                    | $< 20$  | $< 13.69$                                    |
| Fe II   | 1144.938           | 0.106  | $< 15$  | $< 13.12^d$                                  | $< 21$  | $< 13.23$                                    |

Note. — \* Because some saturation is indicated in the line profile, the total column density may be slightly higher.

<sup>a</sup>Wavelengths and oscillator strengths are from D. C. Morton (2003, in preparation).

<sup>b</sup>Unless otherwise specified, column densities are calculated through the apparent optical depth method. All upper limits are  $3\sigma$  levels.

<sup>c</sup>H I column densities are calculated through a curve-of-growth analysis of Lyman series lines in the *FUSE* bandpass.

<sup>d</sup>Column density is calculated through a curve-of-growth analysis of low-ionization species. The data is best fitted by a curve of growth with doppler parameter,  $b = 10.3^{+6.5}_{-2.9} \text{ km s}^{-1}$ .

Table 3. PKS 2155–304 H I MEASUREMENTS

| Line          | $\lambda(\text{\AA})$ | $f^a$    | Equivalent Width ( $W_\lambda$ in m $\text{\AA}$ ) |   |
|---------------|-----------------------|----------|--|---|
|               |                       |          | –140 km s $^{-1}$<br>Component <sup>b</sup>        | –270 km s $^{-1}$<br>Component <sup>c</sup> |
| Ly $\gamma$   | 972.537               | 0.0290   | ...  | $87 \pm 12$                                 |
| Ly $\delta$   | 949.743               | 0.0139   | ...  | $61 \pm 10$                                 |
| Ly $\epsilon$ | 937.803               | 0.00780  | ...  | $59 \pm 11$                                 |
| Ly $\zeta$    | 930.748               | 0.00481  | ...  | $35 \pm 12$                                 |
| Ly $\eta$     | 926.226               | 0.00318  | $132 \pm 10$                                       | ...   |
| Ly $\theta$   | 923.150               | 0.00222  | $122 \pm 10$                                       | ...   |
| Ly $\iota$    | 920.963               | 0.00161  | $113 \pm 10$                                       | ...   |
| Ly $\kappa$   | 919.351               | 0.00120  | $95 \pm 10$  | ...   |
| Ly $\lambda$  | 918.129               | 0.000921 | $87 \pm 10$  | ...   |

<sup>a</sup>Wavelengths and oscillator strengths are from D. C. Morton (2003, in preparation).

<sup>b</sup>The data are best fitted by a curve of growth with doppler parameter  $b = 13.9_{-2.3}^{+3.1}$  km s $^{-1}$  with  $\log N(\text{H I}) = 16.37_{-0.14}^{+0.22}$ .

<sup>c</sup>The data are best fitted by a curve of growth with doppler parameter  $b = 8.0_{-2.0}^{+3.5}$  km s $^{-1}$  with  $\log N(\text{H I}) = 15.23_{-0.22}^{+0.38}$ .

Table 4. SUMMARY OF MEASUREMENTS: Mrk 509

| Species | $\lambda^a$<br>(Å) | $f^a$  | Component 1   |  | Component 2   |  |
|---------|--------------------|--------|---|--|---|--|
|         |                    |        | $V_{LSR} = -240 \text{ km s}^{-1}$<br>$W_\lambda$<br>(mÅ) | $\log N(X)^b$<br>( $N$ in $\text{cm}^{-2}$ ) | $V_{LSR} = -300 \text{ km s}^{-1}$<br>$W_\lambda$<br>(mÅ) | $\log N(X)^b$<br>( $N$ in $\text{cm}^{-2}$ ) |
| H I     | ...                | ...    | ...   | $< 17.69^c$                                  | ...   | $< 17.69^c$                                  |
| C II    | 1036.337           | 0.118  | $< 23$  | $< 13.32$                                    | $48 \pm 10$   | $13.68^{+0.08}_{-0.09}$                      |
|         | 1334.532           | 0.128  | $< 25$  | $< 13.15$                                    | $88 \pm 12$   | $13.73^{+0.05}_{-0.06}$                      |
| C IV    | 1548.203           | 0.190  | $100 \pm 13$  | $13.53^{+0.05}_{-0.06}$                      | $264 \pm 18$  | $14.15^{+0.10}_{-0.07}^d$                    |
|         | 1550.770           | 0.0948 | ...   | ...  | $184 \pm 19$  | ...  |
| N I     | 1199.550           | 0.130  | $< 41$  | $< 13.38$                                    | $< 58$  | $< 13.53$                                    |
| N V     | 1238.821           | 0.157  | $< 25$  | $< 13.08$                                    | $< 36$  | $< 13.24$                                    |
| O I     | 1302.169           | 0.0519 | $< 22$  | $< 13.47$                                    | $< 32$  | $< 13.62$                                    |
| O VI    | 1031.926           | 0.133  | $77 \pm 6$  | $13.89^{+0.04}_{-0.04}$                      | $86 \pm 10$   | $13.93^{+0.04}_{-0.05}$                      |
| Si II   | 1193.290           | 0.585  | $< 53$  | $< 12.93$                                    | $< 72$  | $< 13.09$                                    |
| Si III  | 1206.500           | 1.669  | $49 \pm 12$   | $12.44^{+0.10}_{-0.12}$                      | $194 \pm 19$  | $13.31^{+0.03*}_{-0.04}$                     |
| Si IV   | 1393.755           | 0.514  | $< 24$  | $< 12.49$                                    | $113 \pm 11$  | $13.53^{+0.19}_{-0.13}^d$                    |
|         | 1402.770           | 0.255  | $< 29$  | $< 12.84$                                    | $84 \pm 12$   | ...  |
| S II    | 1253.801           | 0.0109 | $< 11$  | $< 13.85$                                    | $< 15$  | $< 14.00$                                    |
| S III   | 1012.495           | 0.0442 | $< 23$  | $< 13.78$                                    | $< 33$  | $< 13.93$                                    |
| Fe II   | 1144.938           | 0.106  | $< 27$  | $< 13.21$                                    | $< 39$  | $< 13.37$                                    |

Note. — \* Because some saturation is indicated in the line profile, the total column density may be slightly higher.

<sup>a</sup>Wavelengths and oscillator strengths are from D. C. Morton (2003, in preparation).

<sup>b</sup>Unless otherwise specified, column densities are calculated through the apparent optical depth method. All upper limits are  $3\sigma$  levels.

<sup>c</sup>The upper limits on  $\log N(\text{H I})$  are  $4\sigma$  levels from Sembach et al. (1995).

<sup>d</sup>Column density is measured by the CoG doublet method.

Table 5. LOGARITHMIC COLUMN DENSITY RATIOS

| Ratio                             | PKS 2155–304 <sup>a</sup>            |                                      | Mrk 509 <sup>b</sup>                 |                                      | Complex C <sup>c</sup> |
|-----------------------------------|--------------------------------------|--------------------------------------|--------------------------------------|--------------------------------------|------------------------|
|                                   | –140 km s <sup>–1</sup><br>Component | –270 km s <sup>–1</sup><br>Component | –240 km s <sup>–1</sup><br>Component | –300 km s <sup>–1</sup><br>Component |                        |
| $N(\text{H I})/N(\text{O VI})$    | $2.57^{+0.22}_{-0.14}$               | $1.67^{+0.38}_{-0.23}$               | < 3.80                               | < 3.76                               | $6.38^{+0.05}_{-0.05}$ |
| $N(\text{O I})/N(\text{O VI})$    | < –0.40                              | < –0.05                              | < –0.42                              | < –0.31                              | $2.21^{+0.19}_{-0.25}$ |
| $N(\text{Si II})/N(\text{Si IV})$ | $0.07^{+0.14}_{-0.13}$               | < 0.51                               | ...                                  | < –0.44                              | $2.03^{+0.22}_{-0.20}$ |
| $N(\text{C II})/N(\text{C IV})$   | $0.36^{+0.11}_{-0.08}$               | < –0.56                              | < –0.38                              | $-0.44^{+0.11}_{-0.09}$              | ...                    |
| $N(\text{C IV})/N(\text{Si IV})$  | $0.74^{+0.08}_{-0.09}$               | $1.30^{+0.12}_{-0.16}$               | > 1.04                               | $0.62^{+0.21}_{-0.15}$               | $0.59^{+0.12}_{-0.15}$ |
| $N(\text{C IV})/N(\text{N V})$    | > 0.40                               | > 0.47                               | > 0.45                               | > 0.91                               | > 0.07                 |
| $N(\text{O VI})/N(\text{C IV})$   | $0.32^{+0.05}_{-0.05}$               | $0.00^{+0.06}_{-0.07}$               | $0.36^{+0.06}_{-0.07}$               | $-0.22^{+0.11}_{-0.09}$              | $0.31^{+0.08}_{-0.09}$ |

<sup>a</sup>The mean of the column densities derived from C IV  $\lambda 1548.2$  and  $\lambda 1550.8$  is used for ratios involving  $N(\text{C IV})$  for the PKS 2155–304 sight line.

<sup>b</sup>The mean of the column densities derived from C II  $\lambda 1036.3$  and  $\lambda 1334.5$  is used for ratios involving  $N(\text{C II})$  for the Mrk 509 sight line.

<sup>c</sup>Values for Complex C are measured along the PG 1259+593 sight line (Collins et al. 2003).

Table 6. MODEL CHARACTERISTICS OF HVCs TOWARD PKS 2155–304<sup>a</sup>

| $Z$                               | $\log N(\text{H I})$<br>( $\text{cm}^{-2}$ ) | $\log U$ | $\log n_{\text{H}}$<br>( $\text{cm}^{-3}$ ) | $\log T$<br>(K) | $P/k$<br>( $\text{K cm}^{-3}$ ) | Size<br>(kpc) |
|-----------------------------------|--|----------|---|-----------------|---------------------------------|---------------|
| –140 $\text{km s}^{-1}$ Component |  |          |   |                 |                                 |               |
| –0.32                             | 16.23  | –3.02    | –3.46                                       | 4.02            | 8.4                             | 2.6           |
| –0.47                             | 16.37  | –3.02    | –3.46                                       | 4.07            | 9.4                             | 4.0           |
| –0.71                             | 16.59  | –3.04    | –3.44                                       | 4.14            | 11.5                            | 6.9           |
| –270 $\text{km s}^{-1}$ Component |  |          |   |                 |                                 |               |
| –0.92                             | 15.01  | –1.98    | –4.50                                       | 4.34            | 1.6                             | 30            |
| –1.20                             | 15.23  | –1.98    | –4.50                                       | 4.38            | 1.7                             | 54            |
| –1.65                             | 15.61  | –1.98    | –4.50                                       | 4.42            | 1.9                             | 140           |

<sup>a</sup>Results from CLOUDY photoionization model calculations. See text for a description of these models.